PUMA, SPSC report on the activities of 2022

Oliver Aberle, Oliver Boine-Frankenheim, François Butin, Paolo Chiggiato,
Jose Ferreira Somoza, Jonas Fischer, Guillaume Hupin, Berthold Jenniger,
Clara Klink, Yuki Kubota, Alexandre Obertelli, Luisa Riik,
Moritz Schlaich, Alexander Schmidt, Erwin Siesling, Anke Stoeltzel,
Frank Wienholtz, Christina Xanthopoulou, Sabrina Zacarias

on behalf of the PUMA collaboration

January 21, 2023

Contents

1 Reminder of objectives for 2022

The PUMA experiment was accepted at CERN in 2021. PUMA is in its construction phase. This document summarises the work performed in 2022, i.e., beyond the content of Ref. [1] where a description of the motivations of PUMA and its status at the end of 2021 can be found. The present report focuses on the design, construction and installation of the experiment. For the SPSC meetings that occurred in 2022, objectives for 2022 for PUMA were mentioned (for example, see slides dated of 29.05.2022, sent to the SPSC of June 2022). As an overview, the milestones of the PUMA project are reported in Tab. 1 and their status is given. Details are given in the following sections of this report.

Working Group	Milestone	Status
ELENA beam line	NEG coating	done
	Assembly of elements	done
	Full beam line installed	done
	Power line on crane installed	done
	Diesel generator purchased and installed	done
	Safety cage and interlock installed	done
	PDT validation	done
	Transmission of antiprotons characterized	reported to Q2/23
Offline ion source	All components received	done
	MR-TOF assembled	done
	Full assembly at TU Darmstadt	reported to Q1/23
	Full operation and validation	reported to Q2/23
Trap	Design finalized	done
	All parts received	reported to Q1/23
	Full trap assembly	reported to Q2/23
	Delivery TPC	reported to Q1/23
	Validation TPC and trigger barrel	reported to Q2/23
ISOLDE beam line	Project officially started	done
	Emittance measurements of low-energy beams	reported to Q1/23
	Simulations	reported to Q2/23
	Final design	reported to Q2/23

Table 1: Milestones foreseen for 2022 and status.

2 The PUMA antiproton beam line at ELENA

The PUMA antiproton beam line aims at slowing down the antiprotons, which are delivered by the ELENA synchrotron, from a kinetic energy of 100 keV to 4 keV, to be able to capture and store them in the PUMA Penning trap system with the highest efficiency possible. For this, a pulsed drift tube (PDT) will be installed and used. Requirements for the design of the beam line are a beam spot size lower than 6 mm FWHM at the trap entrance and an energy fluctuation of less than 100 eV with paired with a transmission efficiency of better than 75%. The beam line was optimized and benchmarked with ion optics simulations to meet these criteria. An overview of the antiproton beam line is shown in Fig. 1. The main related tasks were:

- January - June 2022: construction of beam line, including pulsed drift tube (PDT) and safety cage

- June 2022: electrical safety authorization for operation

- July - October 2022: conditioning of PDT

- November 2022: temporary beam permit

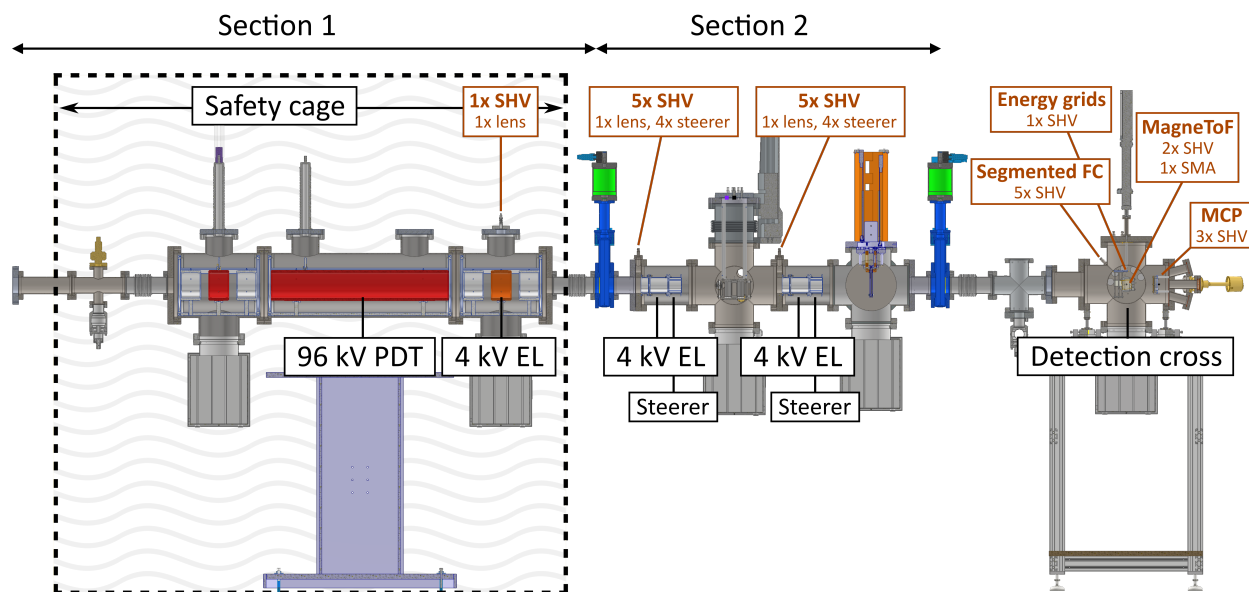- November 2022: commissioning with antiprotons

Figure 1: Half-section view of the current experimental setup, including the necessary electrical feedthroughs from atmosphere to the XHV side. The antiproton spills go from left to right.

2.1 Construction

Figure 1 depicts a half-section view of the currently installed beamline. Section 1 includes the PDT. Section 2 contains the 90-degree bender cross which will be used to introduce ions towards the trap and the beam viewer. A SEM grid will be installed in 2023. At the current stage, the beam viewer is a temporary phosphor screen.

In Fig. 2 a photograph of the beamline can be seen, in which the main parts are highlighted. The handover point is to the right of the safety cage and section 2 on the left. Section 2 consists of ion optical elements to be able to manipulated the decelerated antiprotons and ions, namely two einzel lenses and a junction to be able to connect to the offline ion source. On the dowstream end of the line the detection cross
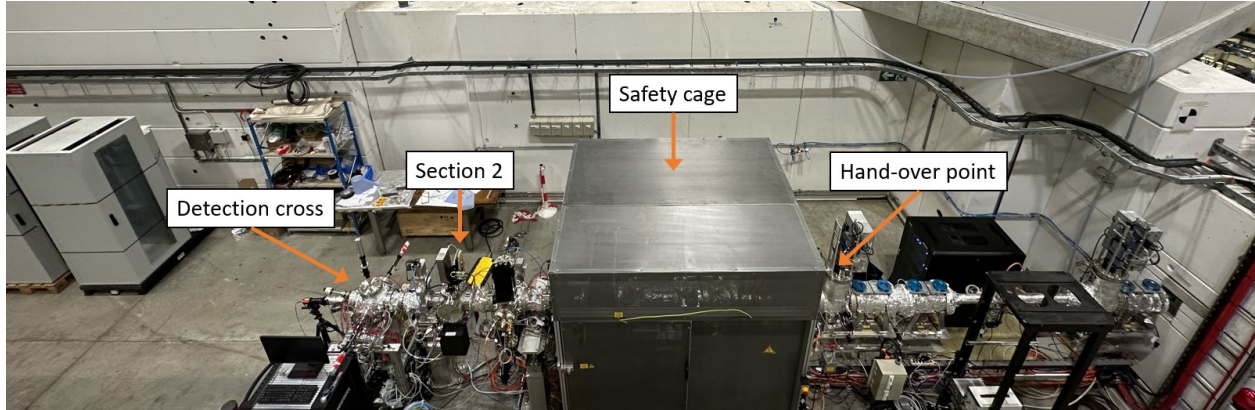
Figure 2: Picture of the beamline.

can be seen.

The pulsed drift tube is connected to the high voltage power supply (Spellman SL130PN60) via a $1\,M\Omega$ resistor (see Fig. 3). To discharge the capacity of the tube quickly, the switch (Behlke HTS 1501-20-LC2) is triggered and the pulsed drift tube is connected to ground via a $500\,\Omega$ resistor. This limits the current that can flow, to make sure that the switch is not damaged.
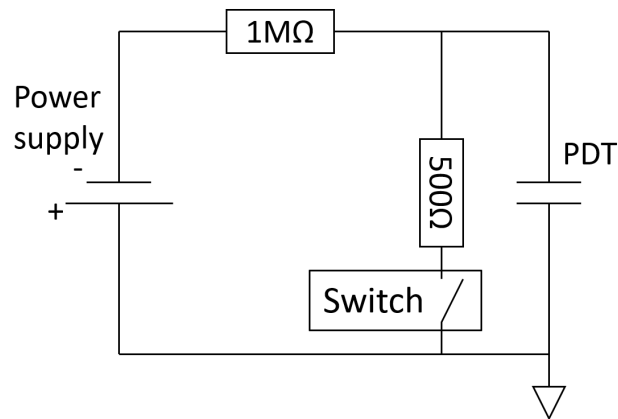
Figure 3: Simplified circuit diagram for the PDT electrical installation.

A measurement of the switching time was done with a 1/1000 voltage divider (LeCroy PPE6kV) connected to a Tektronix MDO3104 scope, switching from $5\,kV$ to ground. Figure 4 shows the trigger signal in yellow and the voltage on the pulsed drift tube in blue. There is a $\sim 200\,ns$ delay which has to be taken into account when switching. The switching time (to 1/e) is $\sim 80\,ns$ and independent of the voltage applied to the switch. This is even slightly better than the time constant estimated by a simple RC-circuit.

$$\tau = RC = 500\Omega \cdot 170pF = 85\,ns \tag{1}$$

Figure 4: Switching time while switching from 5kV to ground, measured with a 1/1000 voltage divider. The trigger signal is shown in yellow and the voltage on the pulsed drift tube in blue.
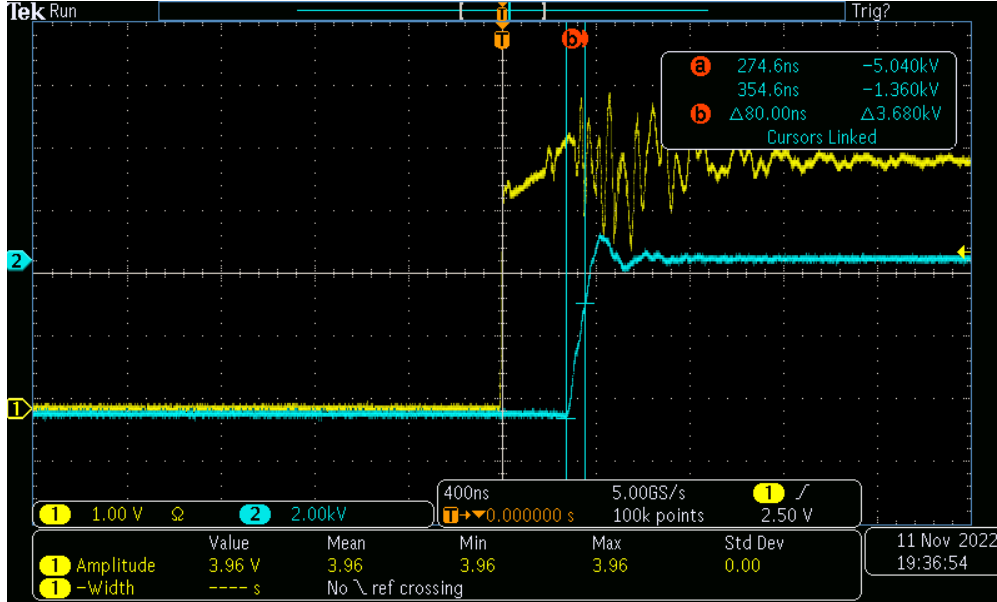
A safety cage was installed around the pulsed drift tube to prevent accidental contact of personnel with the high voltage parts. It is equipped with a trapped key interlock that only allows the operation when the cage is closed and locked. It was developed in close contact with CERN to meet the safety requirements. The high voltage safety cage and everything inside was approved in June for electrical operation. A beam permit for the 2022 beam time was granted in November 2022.

The beamline was baked once after first installation by the CERN Vacuum group to ensure that the NEG activation was working properly. A pressure better than $2 \cdot 10^{-11}$ mbar was achieved. The maximum baking temperature for sections 1 and 2 is 250°C. The beam line was re-opened to install the detection for the in-beam test. The baseline vacuum that achieved in the PDT section was on the order of $1.2 \cdot 10^{-10}$ mbar, without NEG activation. The NEG was not re-activated for the in-beam measurement to conserve peak performance for its operation with the PUMA Penning traps later on. Due to the sensitive detectors, the detection cross was baked at 60° C. Section 1 was pumped by NEG-Ion-combination pump (SAES NEXTorr D2000-10). Section 2 has two ion pumps (Agilent StarCell 300) and the detection cross 1 of the same type.

2.2 Conditioning

The PDT was conditioned over several weeks. Typically, the voltage was increased by 10 kV from 0 to 50 kV, then by 5 kV up to 65 kV. For each voltage, the PDT was left in static operation from half a day to 3 days and monitored. An example of leakage current evolution over 1.5 day for the PDT at 65 kV is shown in Fig. 5. Field emission discharges are visible as current spikes.
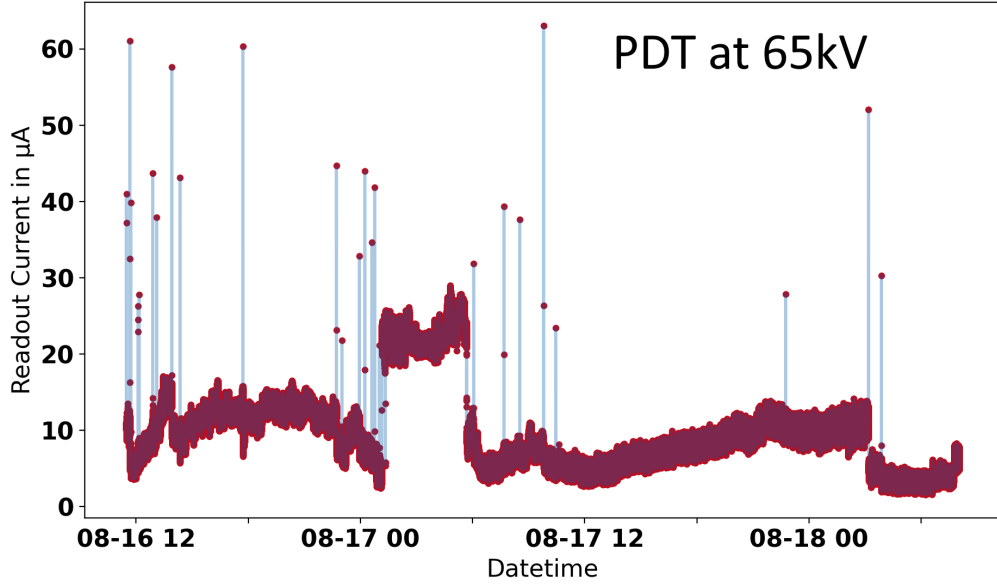
Figure 5: Leakage current of the PDT power supply as a function of time for a conditioning at 65 kV. The Data was taken from August 16, noon, to August 18, 8:00.

From a voltage of 75 kV onward, an increase of the leakage current of the PDT power supply, not correlated with the pressure inside the beam line, showed field emission effects outside the vacuum. These field emissions were lowered to acceptable values, for normal operation of the HV switch controller, by screening of edges which are floated to high voltage and by increasing distances between HV parts and ground. Further improvements along the same course of action are foreseen during the YETS. An overview of the leakage currents for different voltages are shown in Fig. 6. At the end of the conditioning, we were able to reach the goal and sustainably float the PDT to 100 kV.
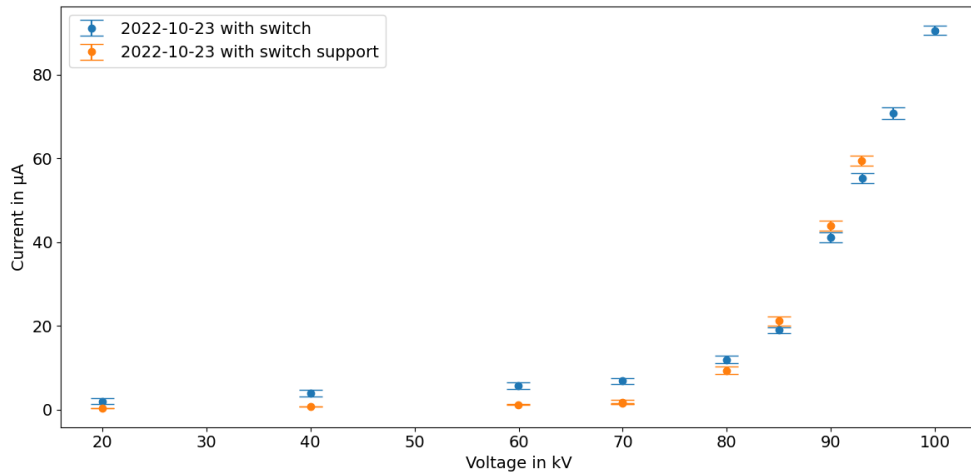
Figure 6: PDT power-supply leakage current versus voltage on the PDT.

2.3 Commissioning of the beamline with antiprotons

Antiproton bunches were taken at PUMA from 15.11 to 22.11 to benchmark the PDT operated at 96 kV and the downstream ion optics. During that beam time, the operation of the PDT was validated and antiproton bunches of 4 keV were characterized. In particular, the bunch length and the energy spread of the antiproton

bunches after the operation of the PDT was measured to be $302\pm20\,\text{ns}$ (FWHM) and $166\pm7\,\text{eV}$ respectively.

The measurements were performed using four different detectors integrated in a single vacuum cross. These are a segmented charge pickup plate, called segmented Faraday cup (sFC) hereinafter, a MagneToF detector, energy analyzer grids (three consecutive metal meshes) and a multi channel plate (MCP) detector, combined to a phosphor screen. A sketch of the detection cross including all four detectors can be seen in Fig. 7. While the MCP is fixed at the end, all other detectors can be moved in and out under remotely using pneumatic feedthroughs.
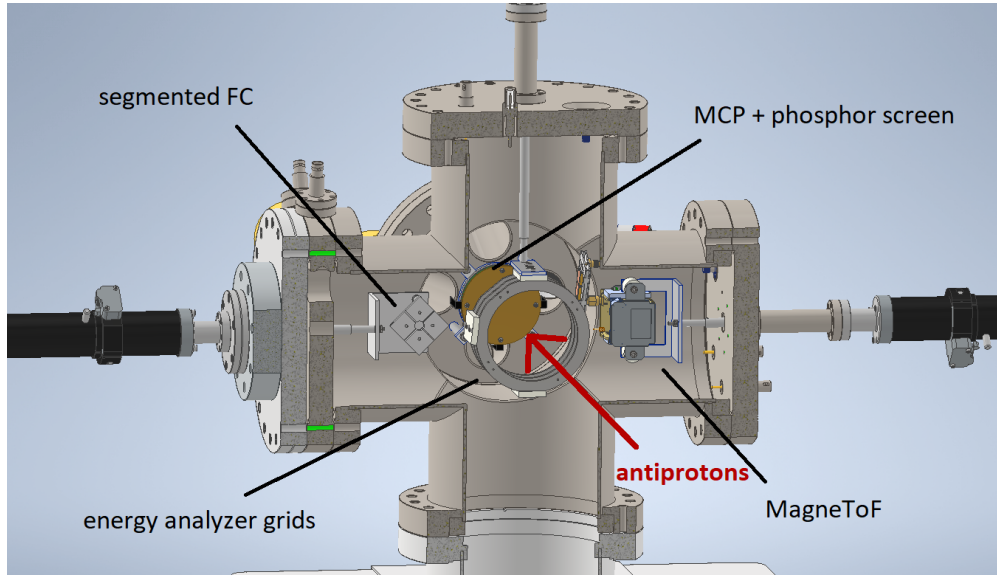

Figure 7: Sketch of the detection cross.

To find the optimal time to trigger the switch, the time delay to the incoming antiproton bunch was varied. When switching too early, the antiprotons see a grounded electrode and continue to travel at their full kinetic energy, thus arriving with the shortest flight time at the detector. When switching too late, the antiprotons are first decelerated when exposed to the 96kV potential of the PDT and subsequently re-accelerated after leaving it. Thus, they will arrive later compared to the situation before. When switching at the correct time, the antiprotons arrive later, as they are now slowed down to 4 kV. A simulation of this can be seen on the left side of Fig. 8, while the measurement is shown on the right panel.
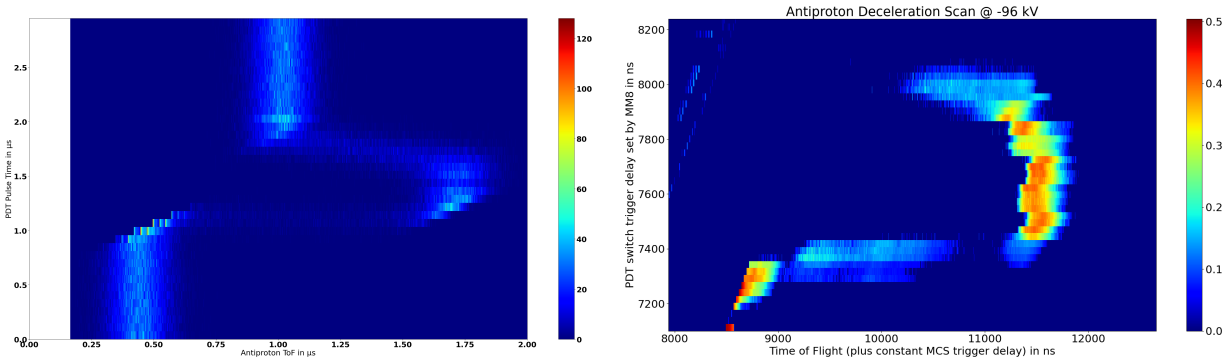

Figure 8: (Left) Simulated time of flight of the antiprotons while scanning the switch trigger delay. Pulsed drift tube switching from -96 kV to ground. (Right) Measured time of flight of antiprotons while scanning the switch trigger delay. Pulsed drift tube switching from -96 kV to ground.

7

3 The offline ion source

The CAD half section view of the offline ion source, supposed to installed at ELENA, is shown on the top panel of Fig. 9. The ion beam will be bent by 90 degrees at the end of this beam line section (not shown) to be able to transfer it to the main beam line, leading to the PUMA Penning traps via a second 90-degree quadrupole bender. These two 90-degree bends not only enable us to use the available space efficiently, but they will also reduce the effect of particle beaming and limit the amount of neutral particles to reach the traps.

The offline ion source is composed of an electron impact plasma ion source, a multi-reflection time of
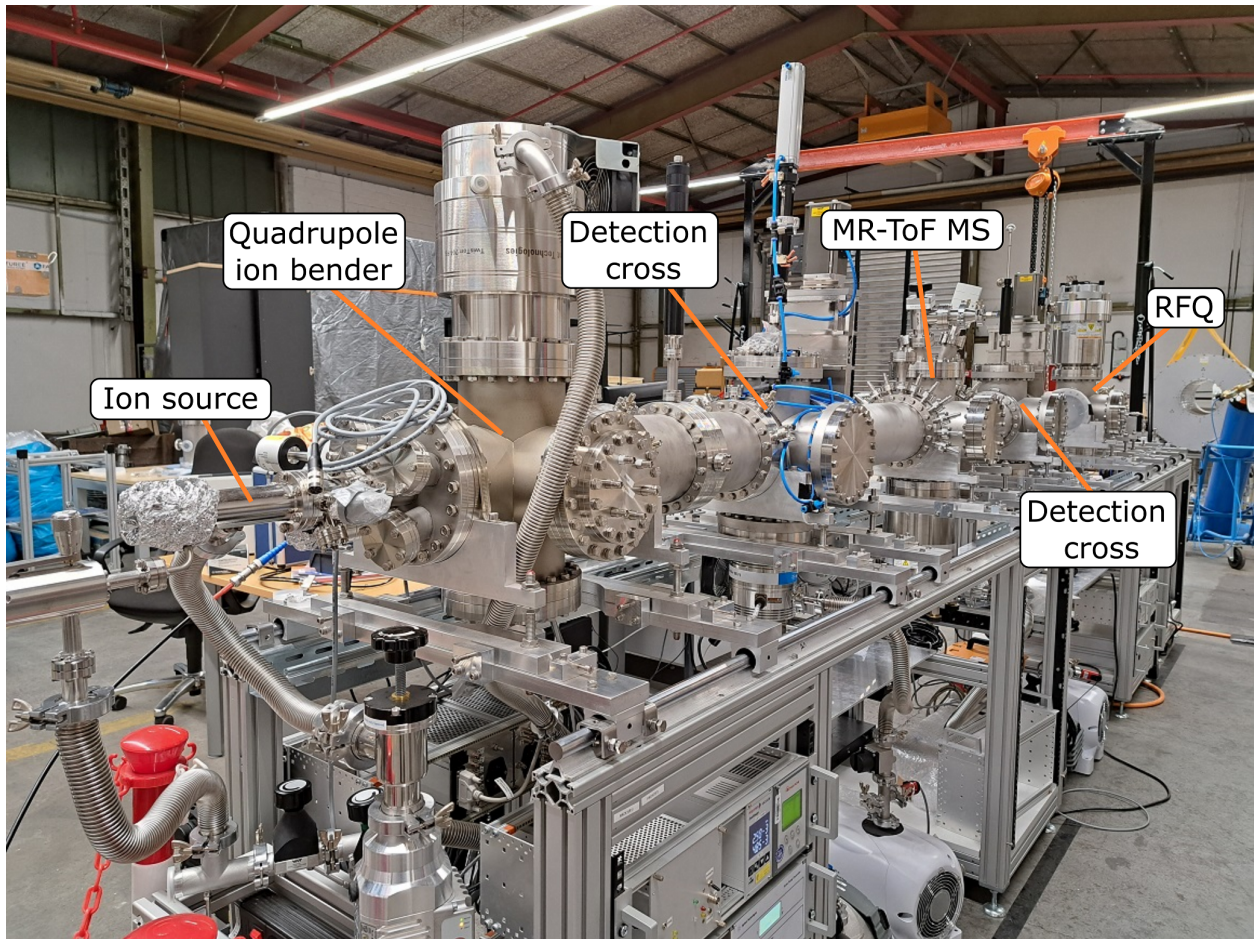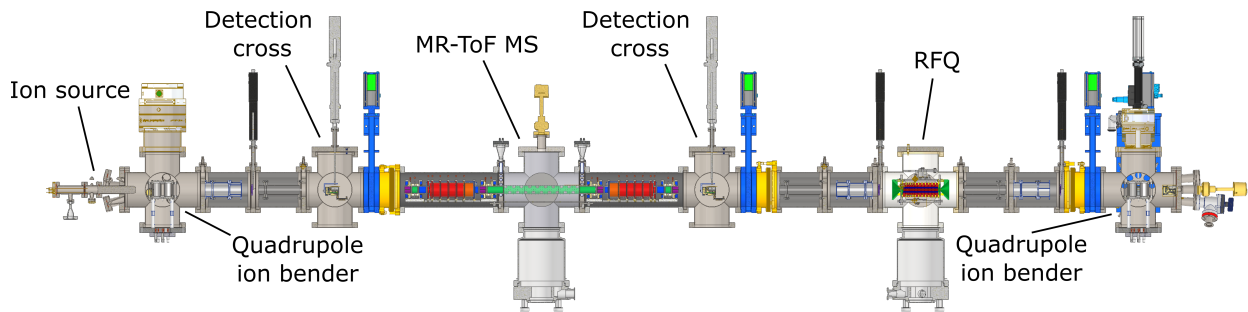

Figure 9: (Top) Technical drawing (side view) of the offline ion source. From left to right: the ion source, the MR-TOF and the RFQ Paul trap are visible. (Bottom) Offline ion source in December 2022 at TU Darmstadt. From left to right: ion source, MR-TOF, RFQ Paul trap and detection cross. See Fig. 11 for details.

flight (MR-TOF) device to select specific isotopes from the source, a RFQ cooler and buncher Paul trap to accumulate ions and form ion bunches, pulsed-drift tubes, focusing and steering elements (einzel lenses) as well as pumping bearers such as externally controllable iris shutters. In 2022, the main related tasks were:

- January - March 2022: end of procurement and first assembly of MR-TOF and RFQ trap

- April - June 2022: PDT, Einzel lenses and Iris shutters assembled and mounted

- July - October 2022: final assembly of MR-TOF and Paul trap, gas inlet for RFQ designed and assembled, control framework developed, first operation of the ions source with H and Ar

- September 2022: move to new laboratory

- October - December 2022: MR-TOF and Paul trap mounted on offline ion source beam line, upgraded gas inlet for ion source designed, built and installed

First tests of the electron impact ion source with argon and hydrogen were performed. For these tests, a Faraday cup and a MagneToF secondary electron multiplier ion detector, which can be used for ToF measurements, was utilized. At the exit of the ion source, a pressure of low 10^{-9} mbar is reached with the source being off. Once the ion source is switched on and an ion current of about 10-50 pA is extracted, the vacuum increases by only a few 10^{-9} mbar. These values are within our specifications since we aim at a vacuum better than 10^{-10} mbar at the injection of the main beamline, well downstream. This objective will be reached with additional pumping and conductance reduction. As an example, Fig. 10 shows beam spots of a 9 pA Ar^+ beam detected with an MCP detector placed 2 m behind the ion source and visualized with a phosphor screen behind it. The beam spot was estimated to have a diameter of approximately 1.5 mm.
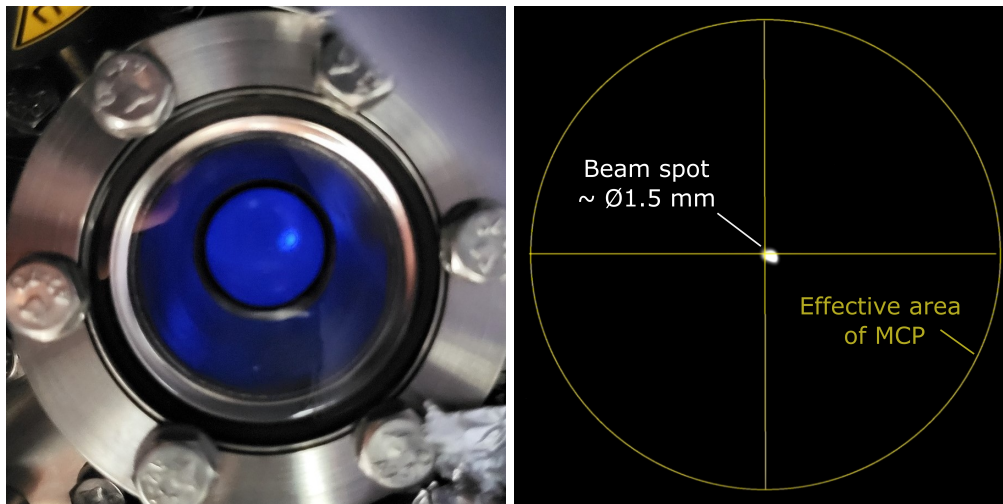
Figure 10: (Left) Picture of an Argon ion beam created with the electron impact plasma ion source, visualized using a phosphor screen located behind an MCP detector. The beam spot is visible on the right side of the screen center. (Right) Beam spot of argon ions focused onto the MCP center. The diameter of the beam spot is approximately 1.5 mm.

The Paul trap and the MR-TOF device have been built, assembled (see Fig. 11), cleaned and mounted in the beam line, together with Einzel lenses for steering and focusing, PDTs and Iris shutters for conductance minimization. The beam line has been baked and a vacuum of few 10^{-9} mbar is reached. For a future modification of the Paul traps buffer gas supply line, an in-vacuum, piezo-driven valve is being designed at the moment. It will allow the buffer gas to flow into the trap only during the ion cooling phase, minimizing the gas injection duty cycle by a factor of 100 or ever more and thus reducing the gas load to the adjunct beamline due to the helium buffer gas by the same factor. A photograph of the ion-source beam line, currently installed at the TU Darmstadt, is shown in the bottom of Fig. 9.

The software and remote control of the beam line is implemented within the CS++ framework based on National Instrument hardware. The CS++ framework was developed at GSI and was adapted and implemented to PUMA with collaborators from GSI. At the end of 2022, a first section of the full beam line including the ion source, lenses and ion detectors was operational. The commissioning and optimization of following sections including the MR-ToF device are scheduled for Q1/23. A few months delay were caused by (i) a move to a new laboratory at TU Darmstadt, which implied a full dismounting and remounting of the beam line in September 2022, (ii) a focus on the commissioning measurements at ELENA.
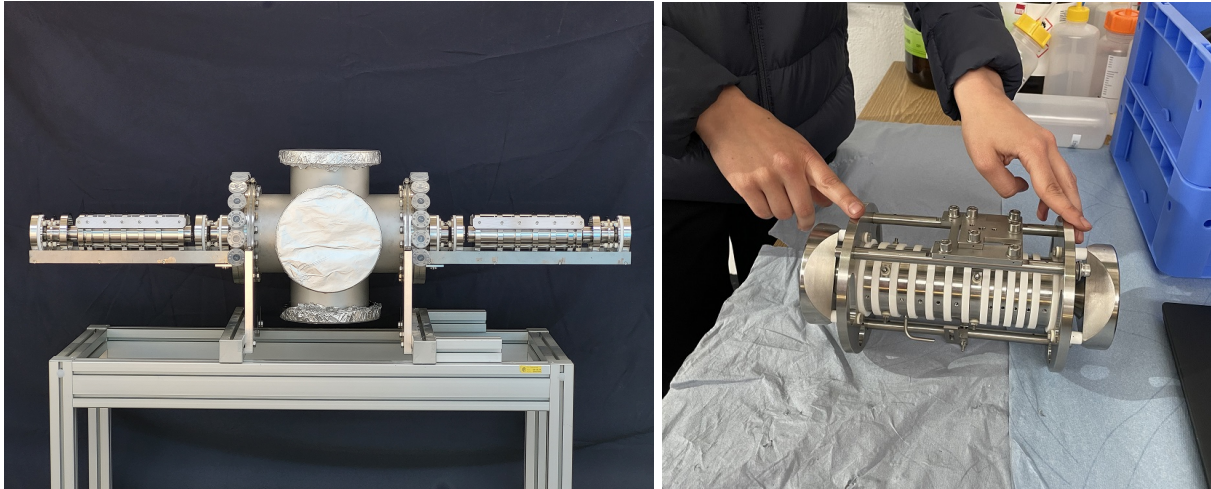
Figure 11: (Left) MR-TOF for isotopic separation of ions coming from the source. The two sets of electrodes forming the electrostatic mirrors are visible. (Right) RFQ cooler and buncher Paul trap for ion accumulation and production of ion bunches.

4 The ion and antiproton traps

4.1 Design and status

A final design of the full trap apparatus including electrodes, mechanical support, cryostat, flanges and vacuum system was validated (see Fig. 12). The validation was performed after vacuum, thermal and mechanical simulations.
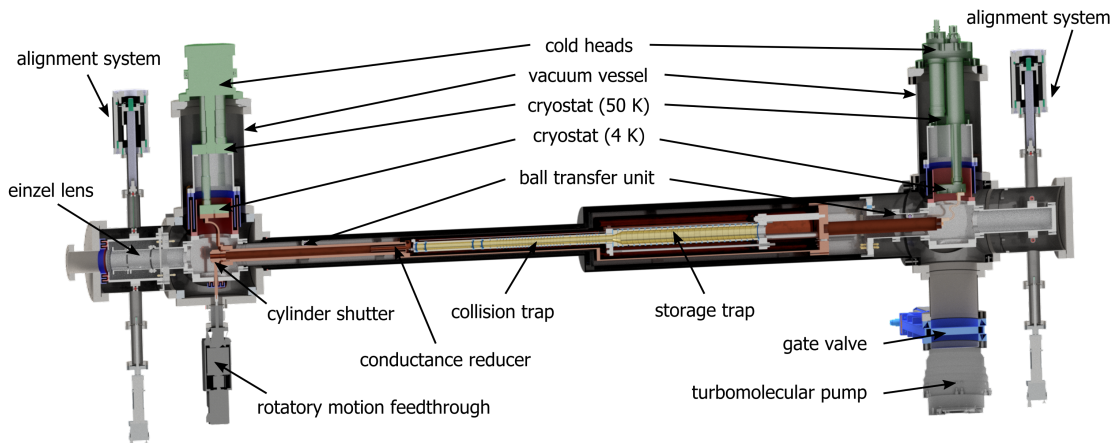
Figure 12: Overview over the final design of the cryostat and Penning trap system of PUMA.

The full vacuum system, in which the trap apparatus is embedded, is composed of a total of 258 individual components (excluding screws, washers, nuts, copper O-rings, etc.), which are distributed over three temperature stages: the 300 K stage as the main vacuum tank (52 pieces), the 70 K stage as temperature buffer and alignment system (80 pieces) and the 4 K stage with the double-trap tower (126 pieces). An overview of the progress for each individual stage is given in Fig. 13. As of 20.01.2023, about 90 % of the parts have been delivered.
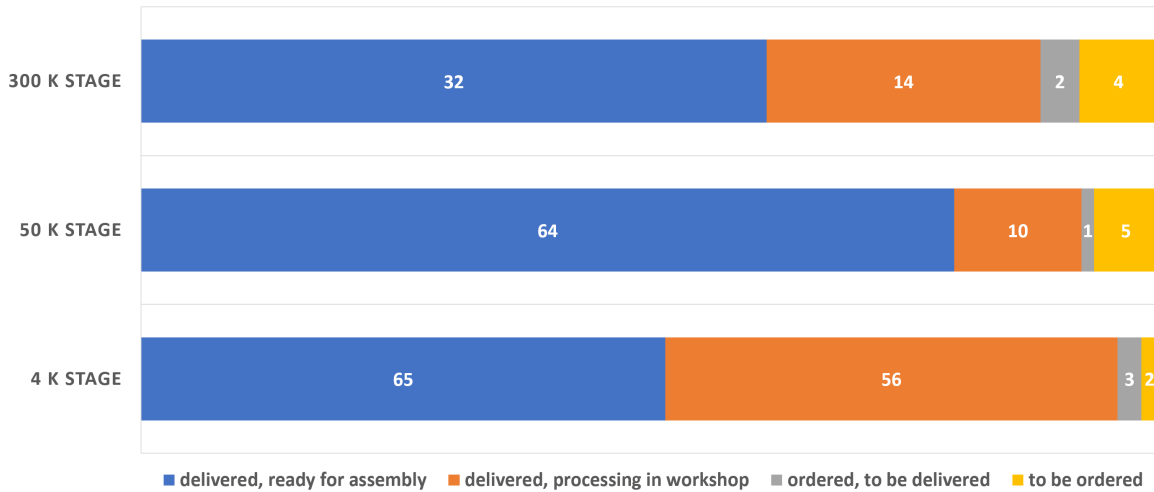
Figure 13: Bar chart of the procurement and manufacturing progress of the different temperature stages of the PUMA vacuum and trap system.

The components that have not been ordered yet are related to the rotating cylindrical beam shutter, which is placed right in front of the cryostat to limit the flux of gas molecules into the trapping region and whose design has been adjusted recently. These adjustments include a segmented pick-up plate, which can be used for steering the antiproton beam while the shutter blocks the entrance to the 4 K cryostat (see Fig. 14) and an XYZ-stage for a fine alignment of the shutter with respect to the cryostat after cooldown over a range of up to ± 5 mm to avoid physical contact while rotating the shutter. In case of contact, the friction of the rotation would cause a burst of gas molecules from the touching surfaces, which would reduce the storage time of antiprotons in the trap significantly. However, even though the shutter does not close up the aperture entirely, the on-axis number density of residual gas molecules is still reduced significantly, as indicated by the simulations depicted in Fig. 14.

Figure 14: Updated concept of the conductance shutter (CS) and its two orientations (left) and its effect on the on-axis residual gas molecule density of the cryostat compared to an uncovered cryostat entrance (right).

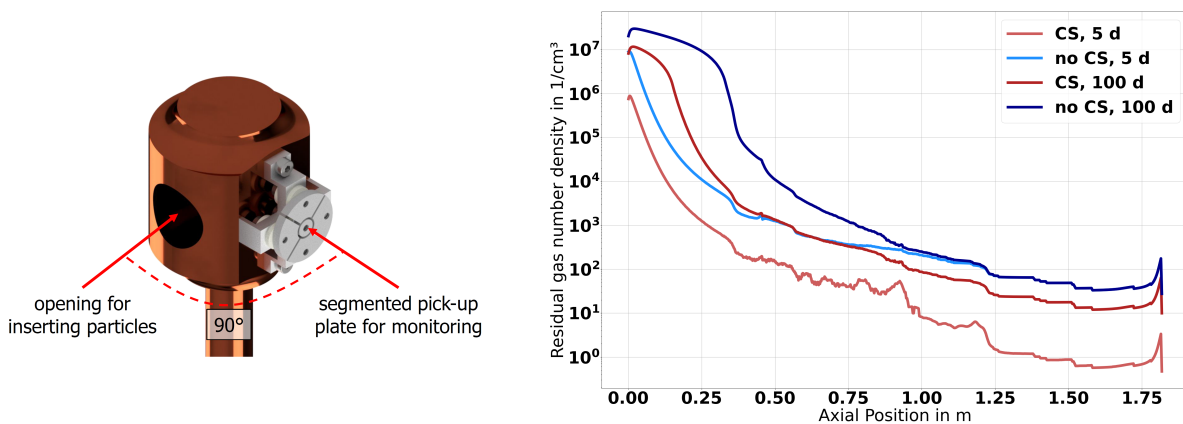There are two main components that have already been ordered but are not yet delivered. One of them is the main vacuum chamber, which will be inserted into the bore of the PUMA solenoid while being surrounded by the pion detection setup. As this chamber requires special dimensions to fit the spatial constraints imposed by the detector and the solenoid bore and a special removable flange for sliding the detector tightly over the tube, the lead time for the chamber has been announced as 6 months. The delivery by Pfeiffer is foreseen for end of February 2023.

The second crucial component is the main chamber of the 4 K cryostat (see Fig. 15). It is composed of three individual subparts - the entrance tube with a high aspect ratio that acts as the initial pressure reducer at the transition to cryogenic temperatures, a small-diameter conductance barrier to further reduce the incoming flux of gas molecules into the trap region and the trap chamber, which houses and supports the double-trap tower. To provide sufficient cooling for the trap electrodes, the main chamber is made out of high-purity oxygen-free electrical (OFE) copper, which has a high thermal conductivity even at cryogenic temperatures. It is supported within the 50 K stage of the setup only by four sets of ball transfer units (BTU) to minimize the heat transfer. These BTUs fix the position of the cryostat in radial direction to prevent a displacement during transport of the setup and are used as roller bearings for inserting the 4 K assembly into the 50 K chamber during the mounting of the setup. Due to the strong constraints set by the BTUs, the outer radius, the circularity as well as the straightness of the three parts are subjected to tight tolerances over the full length. They are currently being manufactured at the mechanical workshop of CERN and the delivery is foreseen for February 2023.

Figure 15: Rendered 3D model of the 4 K cryostat main chamber. The model has been approved by the CERN mechanical workshop and is currently manufactured.

All other components related to the 4 K stage and the trap are already delivered. To check the compatibility of the copper electrodes with the sapphire insulator rings, a test assembly has been performed (see Fig. 16). After the successful test assembly, they will be sent for polishing and plating. The electrical feedthroughs for the trap electrodes are currently welded onto the corresponding base flanges by the mechanical workshop of IKP (TU Darmstadt). In addition, the last mechanical support and alignment pieces are under construction as well.
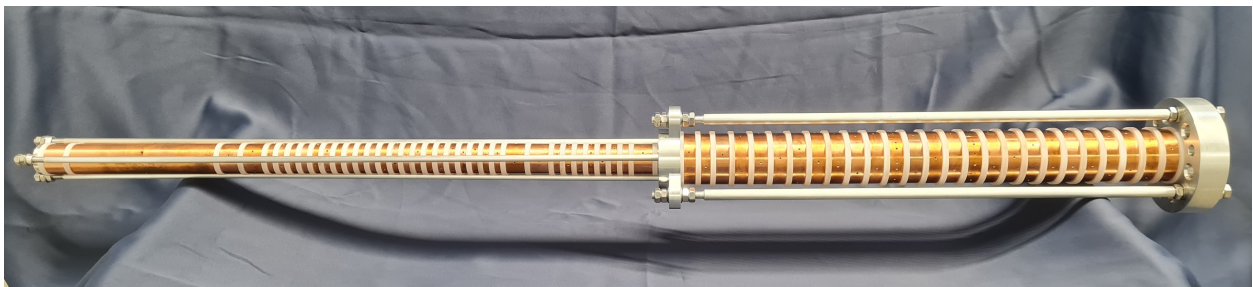
Figure 16: Full trap assembly for mechanical check before polishing and Ag and Au platting.

4.2 Vacuum volume in front of the trap

The vacuum chamber in front of PUMA trap has the role of intercepting the gas coming from the beam line and provide a volume under vacuum in front of the trap that will be transported with it. The chamber consists on a simple NEG coated cross with an aperture of 60 mm with two vertical connections of 100 mm where two Z1000 NEG pumps are installed. The vacuum chamber was tested after coating and the

sticking factor was evaluated as >5e-3 for hydrogen. The final setup, including two sector valves and NEG cartridges, was connected to the test bench (see Fig. 17). The test bench allows the injection of a known flows of hydrogen and measure the pressure on both sides of the cross. The results were compared with those obtained from a 3D simulation with the same assumptions used for the design of PUMA beam line (valve outgassing, NEG coating sticking factor and NEG cartridge pumping speed). The measurement shows values at most 20% less than the data obtained in the simulations, this proves the assumptions were conservative and close to the real values (see Fig. 18).
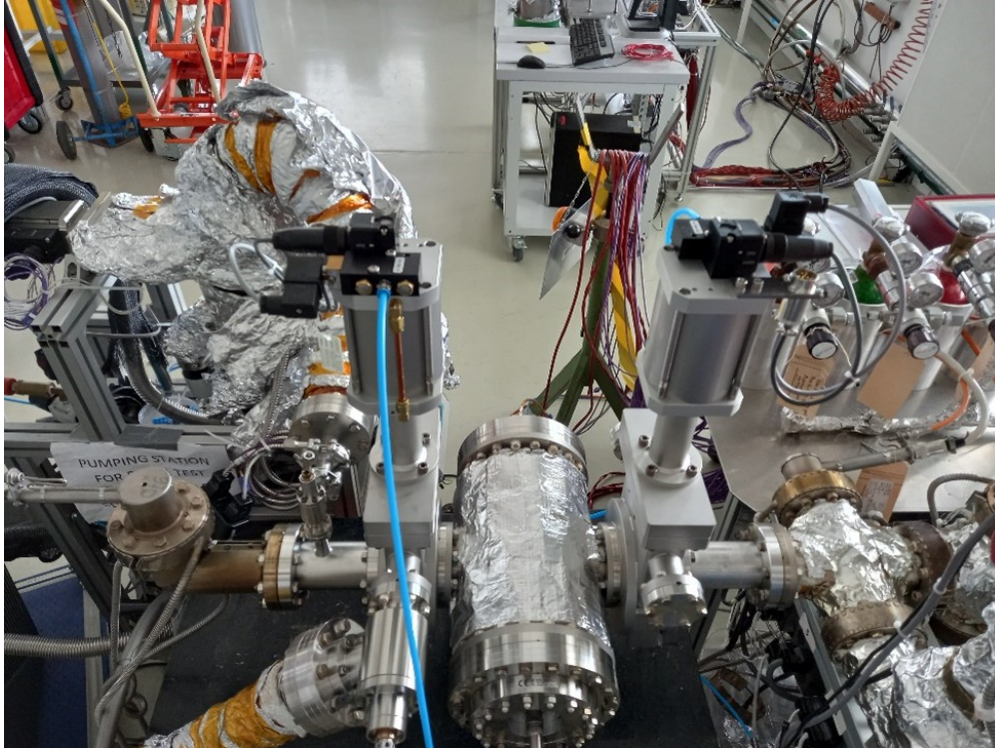
Figure 17: PUMA cross in final configuration connected to a test bench.

5 The time-projection chamber

The main detection of PUMA is composed of a time projection chamber (TPC) surrounded by a barrel of scintillator bars for trigger and timing. A drawing of the final design is shown in Fig. 19. The TPC simulations performed in 2021 converged into the technical design of the detector. The PUMA TPC is being built at CERN by the micro-pattern gas detector (MPGD) group of CERN. The plastic barrel is being developed at TU Darmstadt. The main tasks were

- January - March 2022: Development of a Test Setup for the Trigger Barrel

- March - December 2022: First Validation and Commissioning of the Trigger Barrel Test Setup

- January - July 2022: Finalization of the TPC design

- July - October 2022: Mounting of Anode Test Chamber (Pancake) in the GDD lab

- November 2022: Tests on the TPC Anode Leak current

- February - June 2022: Validation of the TPC FE Electronics

- September - December 2022: Development of an DAQ Interface for the first TPC tests
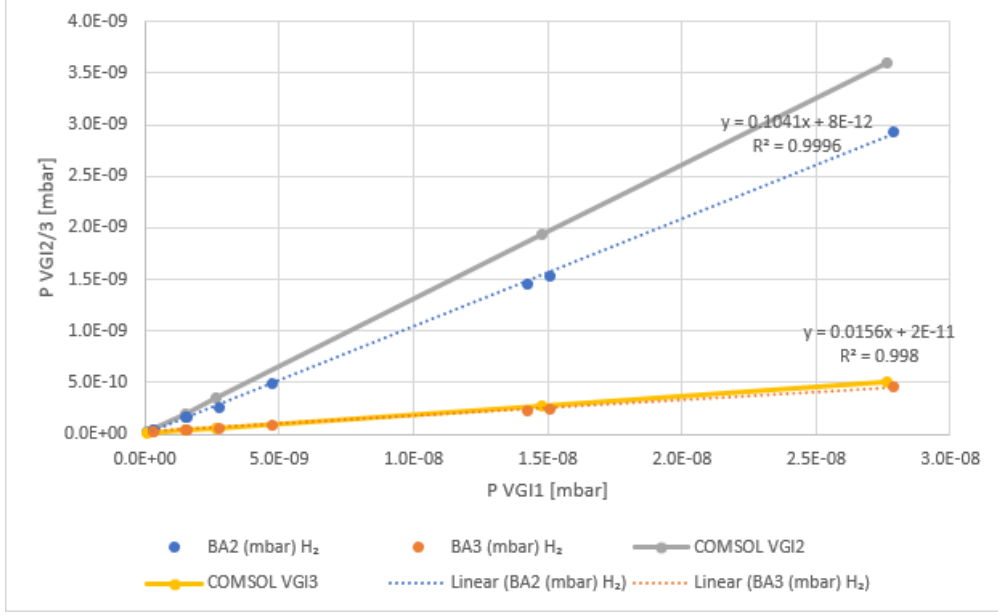
Figure 18: Evaluation of vacuum performance of the vacuum chamber in fron of PUMA trap. Comparison between experimental results (blue and orange dots) and vacuum simulation.
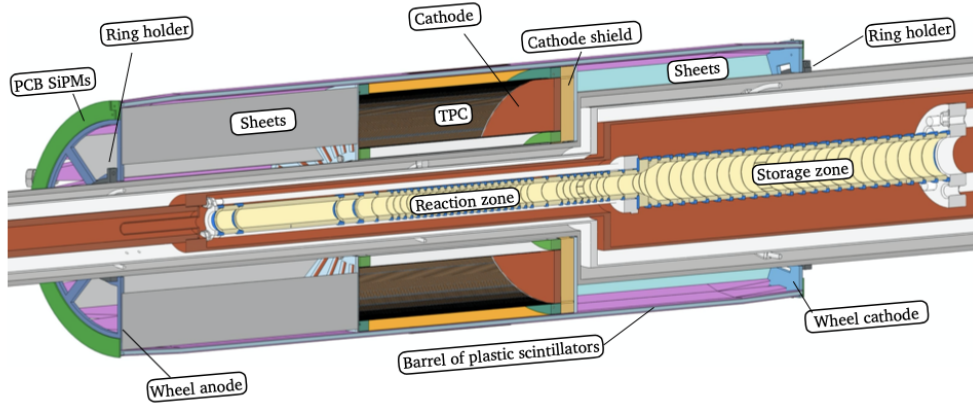
Figure 19: TPC and Plastic scintillators assembled in the beam tube.

Details of the process and full setup are given in the following.

5.1   Cathode and field cage

The cathode is a 10 mm thick copper plate with 1 mm round corners and a 1-100 μm gold- plating (see Fig. 20). The gold plating provides higher conductivity and less degradation of the surface over time than copper. Additionally, the round corners ensure a field strength below the breakdown voltage of air.

The cathode provides the entrance of four gas entrance and exits to the active zone (and additional four at the anode side) and it is shielded from the ground at the inner and outer radius through a 16 mm tick PCB layer. The cathode is screwed into the PCB with 16 M4 screws embedded into the plate.

The field cage structure consists of 200 field shaping strips 1 mm wide with 40 μm rounded edges and 500 μm interstrip, printed at each side of a flexible PCB.The strips on both sides are connected through vias,
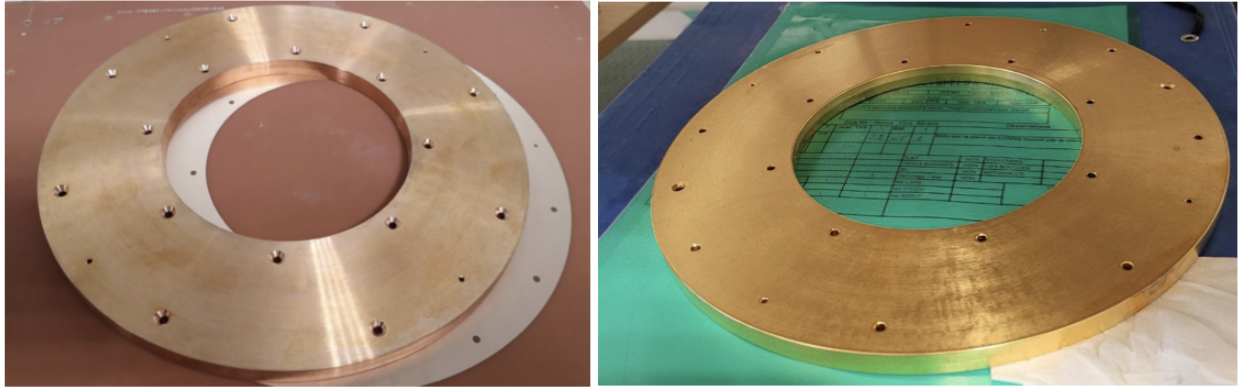
Figure 20: Cathode of the TPC. (Left) Raw material (copper). (Right) Cathode after the gold-coating procedure.

and the degraded potential is achieved by a resistor chain (1 MΩ each) soldered on the outer side of the active volume. The scheme is shown on the left side of Fig. 21 while the manufactured strips are displayed in the middle figure. The first strip of the field cage is connected to the cathode, rendering both at the same potential. An identical resistor chain is installed in case of failure of one of them. A current readout of 10 nA provides sufficient resolution as to determine whether a resistor works at 80% of its nominal operation. The resistors soldered into the PUMA field cage are shown in the right-hand side of the same figure.
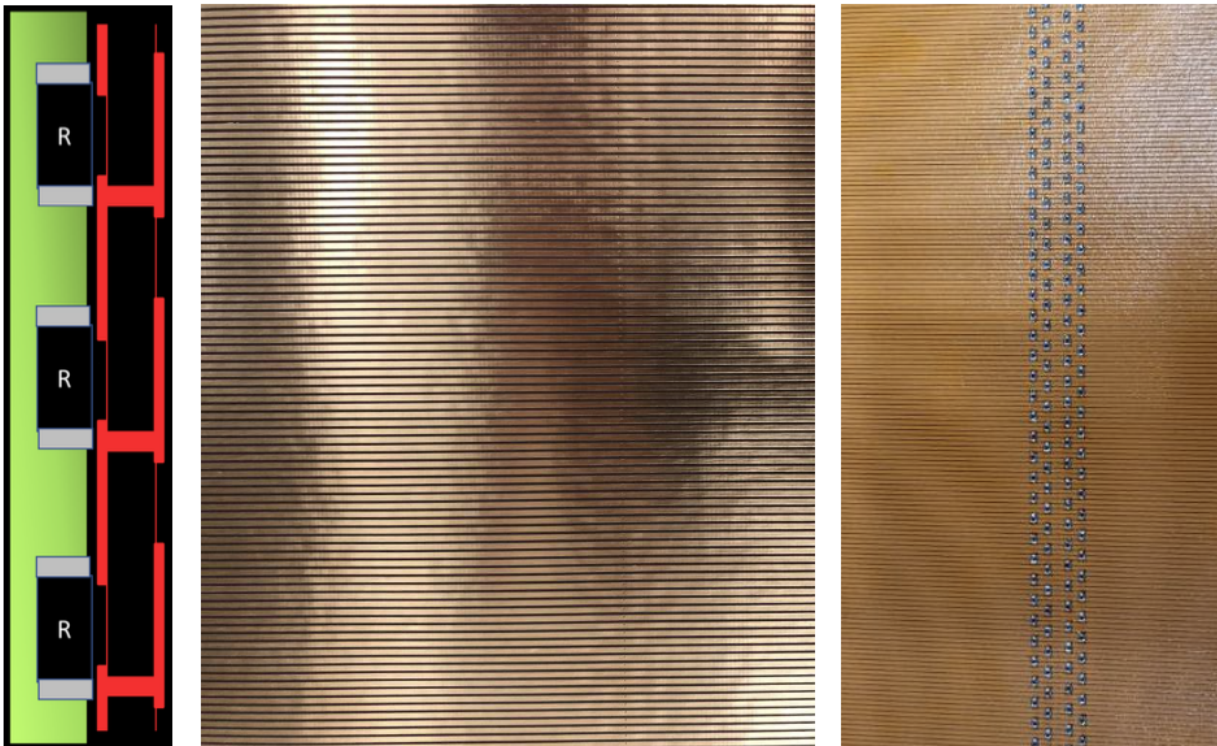
Figure 21: (Left) Strips and resistors scheme. (Middle) TPC Field cage foil from the sensitive volume side. (Right) Detail of the soldered resistor chains on the opposite side of the foil.

5.2   Pad plane

The pad plane geometry (shape and size of pads) was optimized from simulations to maximize the separation efficiency of π^+ and π^-. A radial symmetry was chose, with pads of about 10 mm^2. A separation efficiency of 90% is reached, and a 10% ambiguity for straight tracks.

The final design of the pad plane consists of a total of 4096 channels distributed in 16 sectors. Each sector is formed of 256 channels and read by a single front-end electronics card "Another Readout Card" (ARC) containing four 64 channels STAGE chips. The dead-time of the system is driven by the chip with the highest number of hit channels.

The anode consists of a composite sandwich structure where the top layer is a 50 μm Diamond-Like Carbon (DLC) with a resistance of 10 MΩ per square, used to protect the pad plane from discharges. The DLC, which is at $\sim$500 V, is enclosed in a Faraday cage via the Micromegas mesh and the anode pads. The grounded mesh extends below the field cage internal PCB structure. Three additional layers alternating copper, glue and epoxy make up the charge sharing section and three more layers are used to map the pad plane to the connectors in the backplane.

The manufacturing steps of the anode require, first, the cutting and drilling of the holes of the PCB. After that, the excess debris from the holes is removed by desmear. In this chemical process, the resin remaining is softened with water-based solutions and subsequently the chemical bonds are broken with paramanganate. Finally, a neutraliser is used to remove the permanganate. Once the PCB is cleaned, lithographic techniques are used to etch and print the circuit one layer at a time. The left-hand side of Fig. 23 shows the mask of the backplane, where the holes are vias for the pins of the connectors which need to be etched out.

The middle picture of Fig. 23 shows the back plane of the anode side. The printed layout in radial position of the 32 140-pin connectors for data transfer are observed, each of which is mapped to 128 channels. Additionally, the four 3 mm holes for the entrance/exit of the gas are placed, as well as two points for measuring the current in the mesh. Additional holes for mechanical support are placed in the inner and outer radius.
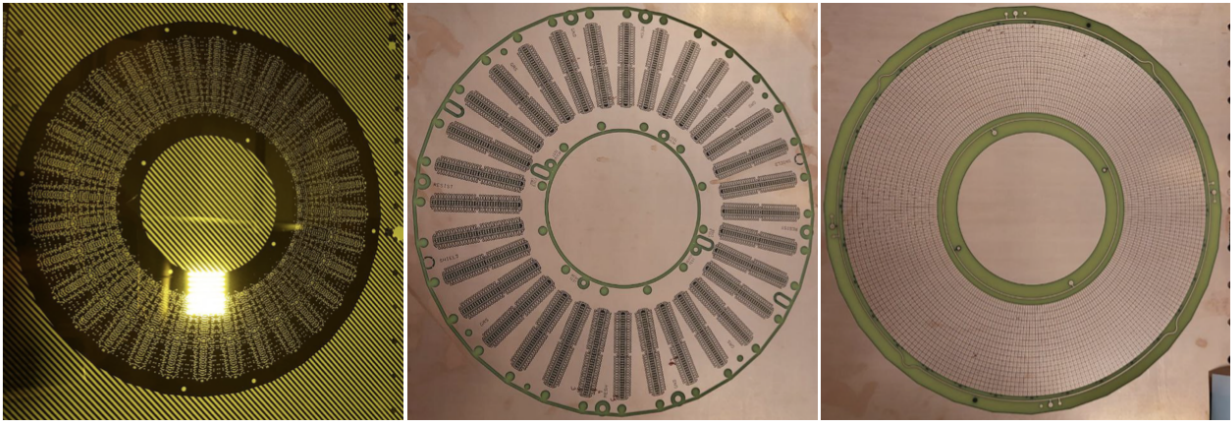
Figure 22: Anode side of the PUMA TPC. (Left) Mask. (Middle) Back plane. (Right) Segmented pad plane.

In Fig. 23 the setup for the first tests on the leakage current of the fully assembled anode in a test setup referred to as the "pancake" is depicted. The voltage was increased step-wise from 200V to 900V aiming for a leak current below 10 nA. This could be confirmed after further cleaning and drying of the device.

5.3   Gas system

The gas system for the PUMA TPC was designed. It must be possible to attach two gas bottles to the TPC since a smaller, lighter gas bottle is needed for the transport to ISOLDE than during normal operation. Before the injection of the gas in the TPC, a pressure reducer and a mass flow controller limit the gas flow to
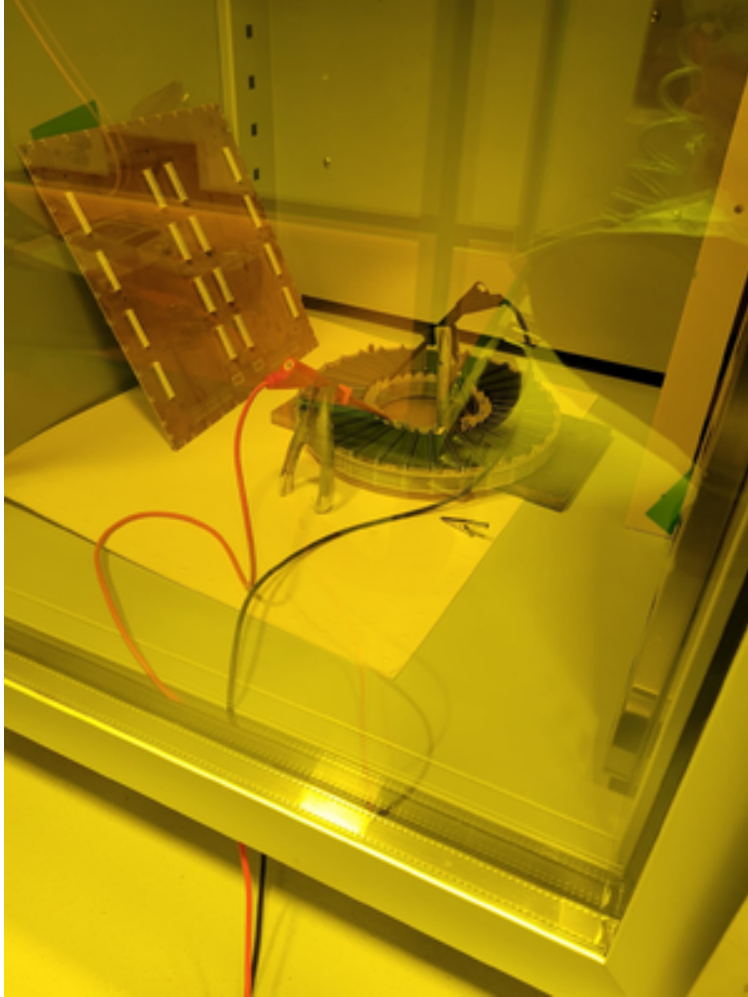
Figure 23: First electrical test of the "pancake".

5-10 L/h in order to flush the TPC regularly. After the TPC, an oxygen and humidity monitor is positioned to allow for correlating the experiments' data with the abundance of residual components in the gas mixture. The schematic setup can be seen in Fig. 24.

The gas has to fulfil several requirements: it must be non-flammable, non-toxic and non-radioactive in order to fulfil CERNs safety protocol. It must operate at a low working voltage and should allow for a high ionisation rate without continuous discharge. Thus, a noble-gas based mixture with quencher must be chosen. Ar-CH4-CO2 (93/5/2) is a mixture that has those properties and also shows low transversal and longitudinal diffusion, and has thus been chosen as the TPC gas [2]. Another candidate is Ar-CO2 (97/3).

5.4   TPC readout and software

The PUMA detector readout system is based on the STAGE chip, which is managed by the ARC boards, and then the data is processed in the trigger and data concentrator module (TDCM). The system was designed at CEA, Saclay. The noise of all of the read-out channels of the STAGE chips was validated at 4.0 ± 0.6 ADC units (maximum signal at 4095 ADC units). A plate for shielding against electromagnetic fields, which would disturb the DAQ, as well as for cooling was developed. The unpacker of the data files with the anode plane signals is based on the transport pipeline package drasi (R3B, GSI).

Figure 24: Gas Handling System schematic overview.

5.5 Trigger barrel

The trigger barrel has the purpose to trigger the anode plane read-out. The barrel reaches also over the storage trap to diagnose antiproton losses in this part of the trap. The plastic barrel is composed of 32 bars made of EJ-212 scintillating organic material. In the final design, th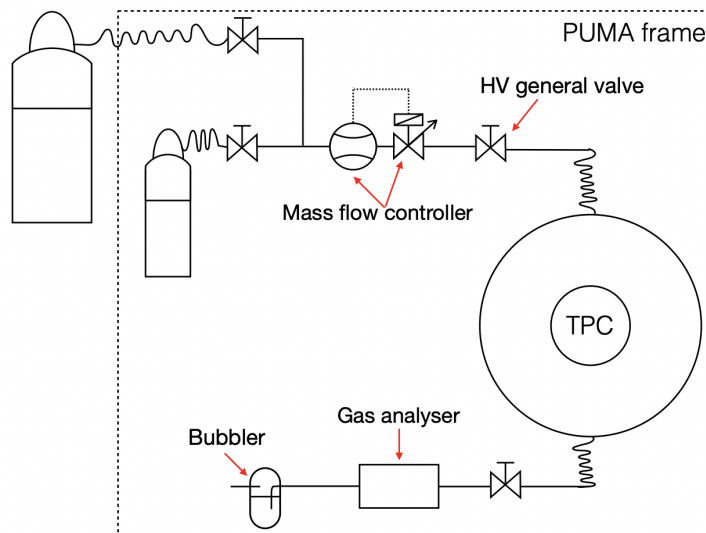e bars will be 1-m long with a thickness of 4 mm. A prototype barrel to be used for the cosmic ray validation of the TPC was developed. Each bar is connected to four SiPM (MICROFC-30050-SMT-T1) so that multiple coincidences are be required to trigger the TPC and the noise triggering was simulated to determine values to reduce it to less than 99.9%. The signals from individual SiPM are collected by concentrator boards (PADIWA4 boards) and the back-end electronics are composed of TRB5sc boards developed at GSI. The electronics scheme is shown in Fig. 25. First validation of the setup were done at TU Darmstadt. One quarter of the prototype barrel is currently mounted and being tested (see Fig. 26).

6 Adsorption isotherm measurements

Available adsorption isotherm data for hydrogen and helium does not cover the range of very low surface coverages sufficiently and therefore predictions of the pressure evolution in the PUMA geometry were uncertain. In order to extend the available data and ensure that vacuum requirements will be met, new adsorption measurements were performed in the laboratory of CERN's vacuum group VSC.

The setup consists of a cryostat, which can be filled with liquid helium, and a bottle-like copper sample, which is encased in an insulation vacuum chamber, which then is emerged in the helium bath. The degradation level of this insulation vacuum and a heating wire installed on the neck of the sample enable measurements at sample temperatures from $4.7\,\mathrm{K}$ to $20\,\mathrm{K}$. Through a long injection line, different gases (H_2, HD, D_2 and He) can be injected into the cold system at the bottom of the sample. Residual gas analyzers are installed at room temperature before the injection line (upstream side) and after the sample, where gas exits the sample neck (downstream side). A turbo-molecular-pump at the downstream side can be connected or valved off, resulting in an open or static system.

Two types of complementary measurements were done. Firstly, adsorption isosteres, which means the curve relating the equilibrium pressure over the surface to the sample temperature at a constant number of
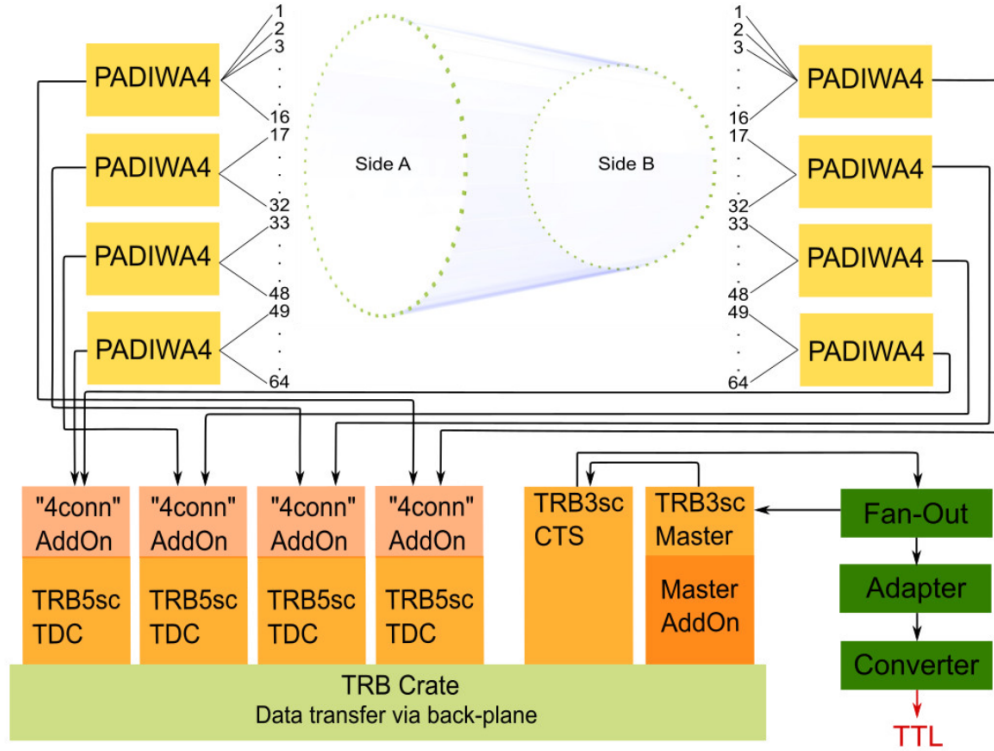
Figure 25: A scheme of the TRB system configuration for the trigger barrel. The numbering referers to the SiPMs attached to the plastic scintillators. The black line between the numbering and the PADIWA4 illustrates the connection of the devices. Side A and B denote each one end of the trigger barrel. Each plastic scintillator has one end cap on each side. The first plastic scintillator has two SiPMs attached on side A defined as A1 & A2 and two on side B defined as B1 & B2. The second scintillator has SiPM A3 & A4 attached on side A and SiPM B3 & B4 attached on side B, and so on. The black arrows illustrate the path of the signals through the TRB system. The final TTL trigger is highlighted by a red arrow.

molecules or atoms adsorbed on the sample surface, i.e. at constant surface coverage. For this measurement, the setup is static and in equilibrium with a homogeneous surface coverage. The Dubinin-Radushkevich-Kaganer (DRK) isotherm model is the most probable model to be valid in the range of low sub-monolayer coverages and has two free parameters: the monolayer capacity S_m and a quantity related to the binding energy of the molecule/atom to the surface, which can be expressed in a temperature T_0. After measuring several isosteres at different coverages, the DRK model is fit to the combined measured data and values for the two parameters can be obtained. The decision to measure isosteres ($p = f(T, \Theta = const.)$) instead of isotherms ($p = f(\Theta, T = const.)$) is justified by the fact that they are part of the same model, but that measurements at low coverages, as expected in PUMA, can be done more easily at higher temperatures with isosteres. The second type of measurement is a gas propagation at a constant sample temperature, where the setup remains open to the pump, the temperature is kept at a desired value and a continuous, constant flow of molecules is injected. Molecules first cover the bottom of the sample, then slowly a pressure front will move upwards until it is detectable at the downstream side. The shape of the pressure front and time when it arrives then gives information about the adsorption process itself. Especially, this measurement can be replicated in COMSOL simulations, using the isotherm parameters obtained by the isostere data fit, and then compared to the measured pressure evolution. This can verify the validity of the isotherm parameters in a different, independent type of measurement.

A snapshot of the current status of these measurements is shown in Fig. 27. In the top row, all current
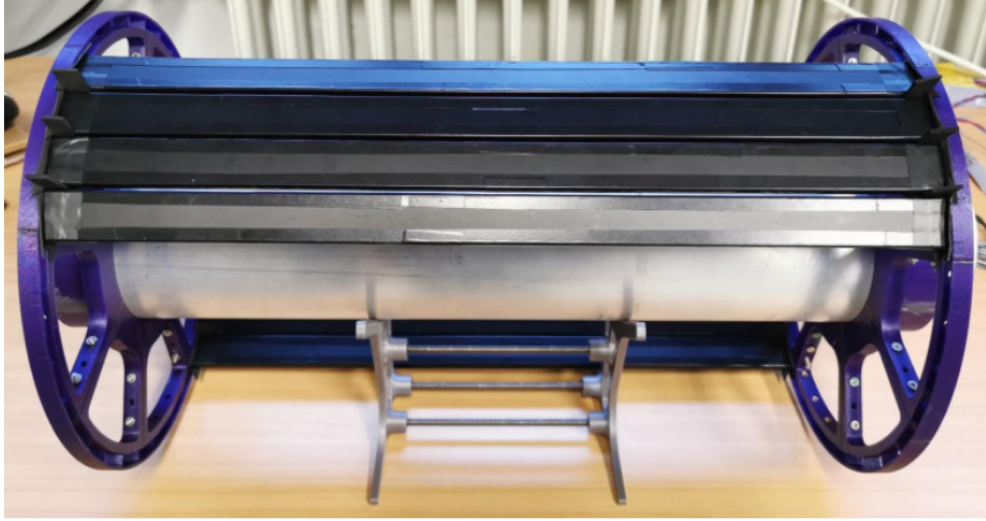
Figure 26: Trigger barrel prototype (1/4) with no SiPM connected.

isostere data for hydrogen and helium are shown. The data sets have been fit to the DRK model, giving only two free parameters for each gas. The DRK model performs well for both helium and hydrogen and represents the data acceptably, within the uncertainties of the measurement, across eight orders of magnitude in pressure. The model appears to be to valid in the very low coverage range studied and no unexpected phenomena in the adsorption process could be found.

The gas propagation measurements (see lower row of Fig. 27) confirm these findings, as the measured pressure evolution can be reproduced by a COMSOL simulation using the adsorption isotherm parameters as found in the fits.

The DRK parameters found in these new measurements so far are $T_{0_{He}} = 74.6 \, \mathrm{K}$ and $S_{m_{He}} = 1.70 \cdot 10^{19} \, \mathrm{m}^{-2}$ and $T_{0_{H_2}} = 205 \, \mathrm{K}$ and $S_{m_{H_2}} = 2.67 \cdot 10^{19} \, \mathrm{m}^{-2}$. These differ slightly form current literature. For helium, measurements performed by Wallen in [3] find $T_{0_{He, \, Wallen}} = 67.2 \, \mathrm{K}$ and $S_{m_{He, \, Wallen}} = 1.72 \cdot 10^{19} \, \mathrm{m}^{-2}$. For hydrogen, the most recent data by Chill, Wilfert and Bozyk [4] find $T_{0_{H2, \, CWB}} = 209.2 \, \mathrm{K}$ and $S_{m_{H2, \, CWB}} = 6.45 \cdot 10^{18} \, \mathrm{m}^{-2}$. The newly obtained isotherm parameters predict a better vacuum in the PUMA trap than the literature values used for simulations in the design phase. Further margin will be obtained with the aC-coating of the trap entry.

Lastly, anti-proton lifetime data, provided by the ALPHA collaboration and measured in the catching trap in the 2021 experimental run, was compared to COMSOL simulations of the trap with the same literature values for the adsorption isotherm as used for the PUMA simulations. The result here too was that the vacuum in the ALPHA catching trap was better than simulated and supports the conclusion that previous estimated were conservative.

7 Non-neutral plasma simulations

The general objectives of plasma simulations for PUMA are, first of all, to deepen the understanding of applied manipulation techniques and to provide fast predictive models with emphases on stability and control of the plasma, thereby facilitate the setup and adjustment of the experimental parameters.

In 2022, the first simulation tools were developed and a collaboration on PUMA with Prof. Katharina Kormann from Ruhr Universität Bochum, Germany, was initiated. As a starting point the complexity should be reduced as much as still reasonable. In the first instance the trapped plasma can be approximated by an infinitely long plasma column. From this there are two options to follow. On the one hand the 1D
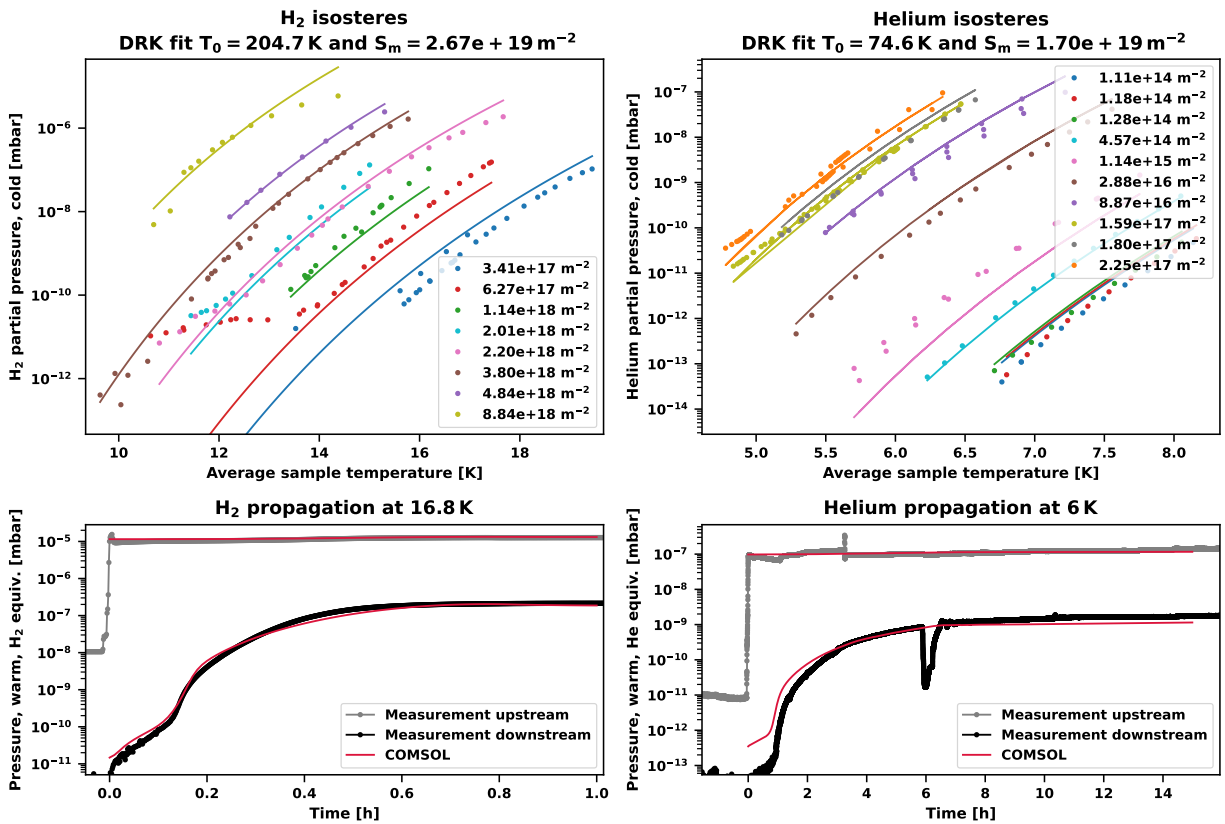
Figure 27: Left column: Hydrogen measurements, right column: Helium measurements. Top row: Isostere data plotted together with DRK fit, bottom row: gas propagation measurement compared to COMSOL simulation with DRK parameters found in the fit of the row above.

longitudinal dynamics can be investigated. On the other hand, by means of the guiding center approximation there exist reduced 2D models for transverse dynamics.

7.1   2D Drift-Kinetic Approximation of Non-neutral Plasma

The reduced 2D model for PUMA was developed and implemented within the scope of a master thesis on PUMA. Its initial purpose was to investigate the rotating wall technique as one of the key techniques for plasma stability. As it turned out, this effect requires coupling to the longitudinal dynamics. But this was out of scope of a master thesis and will now be addressed as part of a subsequent PhD. The master thesis concentrated on purely transversal effects, like the diocotron modes and the stability properties of arbitrary transversal profiles.

The followed simulation approach approximates the continuous density in the 2D drift-Poisson equations by a finite number of macro-particles. The forces between the macro-particles are then calculated by the Fast Multipole Method, a particle-particle method which computational costs scale with $\mathcal{O}(N)$.

The results of the simulation were compared to linear stability analysis. The calculation of the rotation frequency of the plasma column as well as the frequency and grow rates of diocotron modes could be verified, together with the evolution of average radial density profiles in case of multimode excitation. The range of applicability for PUMA is, however, rather limited. Only purely transversal effects can be considered and for multi-species plasma the model is only valid in case of weak partial centrifugal separation. Besides, finite length effects are not included as well as possible B-field gradients, wall resistivity, collisions and so on. Nevertheless, the results obtained by this simulation model can be used as a comparison for higher dimensional codes.

7.2   Rotating Wall Technique

The radial control of particles by the rotating wall technique will be investigated. Kiwamoto et al. [5] showed that the description of radial transport in a Penning-Malmberg trap by a rotating wave requires all 3 space coordinates and the axial velocity. Therefore a four-dimensional code will be implemented. Again the guiding center approximation will be used and an infinitely long plasma column assumed. The rotating wall will be represented by a helically traveling, small amplitude wave perturbation. This will be done in collaboration with Prof. Kormann. The Maxwell-Vlasov equations are implemented with Geometric ElectroMagnetic Particle-In-Cell Methods (GEMPIC)[6] developed at Max-Planck-Institut für Plasmaphysik.

7.3   Autoresonant Excitation

Another task that will be tackled this year is to simulate plasma manuipulations by the longitudinal electric fields as well as autoresonant excitation. This method will be used in the collision trap in order to avoid the trapping of ions in the side wells of the nested potential. Autoresonance is the capture of an oscillatory, nonlinear system into resonance by applying a chirped frequency perturbation. After capture the amplitude of the oscillation is then proportional to the frequency of the perturbation and one can hence control the kinetic energy of the oscillator.

8   The ISOLDE low-energy beam line

Experiments at ISOLDE are foreseen starting from 2024. The low-energy beam line (RC6) of isotopically pure radioactive beams is under the responsibility of CERN. It is seen as a multipurpose beam line which will first be used by PUMA but can be used by other users. The section downstream the handover point is the PUMA zone. The beam lines in this section section is under the responsibility of the collaboration.

In 2022, a dedicated project and associated team have been formed for the low-energy beam line.

8.1 Space, layout and integration

The location of the future beam line serving PUMA has been agreed on.

In the current scheme, only one position for the PUMA experiment fulfils all the requirements necessary for the proposed setup. The space identified for the PUMA experiment in the ISOLDE hall 170 where it could receive Low Energy RIBs, is the position at the end of the RC6 line, where previously the NICOLE experiment was installed. It requires additional space in the HIE ISOLDE part of the experimental hall for the PUMA set-up itself. The former position of NICOLE would be replaced by the MIRACLS set-up (multi-reflection time-of-flight mass separator, MR-ToF MS) [3]. Originally it was foreseen that MIRACLS would provide RIBs with the necessary beam requirements at the entrance of the PUMA experiment which will be located in the HIE ISOLDE part of the experimental hall.

This proposed location is ideal with respect to the specific case of PUMA as a movable experiment: Spacing and infrastructure is available and overhead crane operation is guaranteed. The opening in the wall necessary to go from the Low Energy RC beamline into the HIE ISOLDE part of the hall, as well as a sufficiently large trench for routing cooling-water hoses already exists.

A layout of the ISOLDE experimental zone is shown in Fig.28. The left part is dedicated to low-energy experiments while the more recent experimental zone (on the right) is dedicated to high energy experiments after re-acceleration by the HIE ISOLDE linear accelerator. A possible layout of the PUMA beam line is schematically represented.
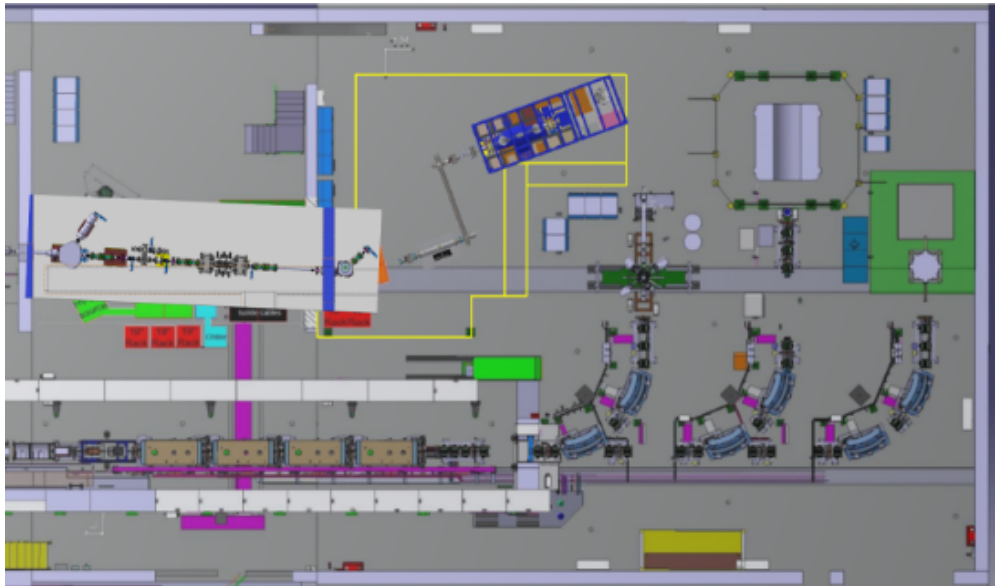
Figure 28: General view of the ISOLDE hall with beam line elements recuperated from MIRACLS and the PUMA experimental area (in yellow).

8.2 Layout of the RC6 beam line

The first part of the RC6 beam line will require beam optics which can be standard ISOLDE electrostatic quadrupole triplets. If standard ISOLDE quadrupoles are recovered from spares the vacuum group would like to explore the option of some improvements or consolidation. In particular UHV cleaning, removing elastomer seals and previous vacuum acceptance tests. For the remaining part and connection to the PUMA setup after the Paul Trap and MR-ToF recovered from MIRACLS, a better vacuum pressure will be required: A chicane vacuum interface will be needed with a minimized mechanical aperture and differential pumping to achieve UHV at entrance to PUMA (better than 10^{-10} mbar). The point where the ISOLDE vacuum

practice no longer applies was defined. After that point, vacuum interventions will require VSC approval, any new instruments will need to be bakeable and tested prior to installation.

As the support from the MIRACLS collaboration will not be available in the future as planned, a reshuffling of elements to build the new beam line had to be done. The EP/SME team did intensive research to identify beam line elements from other experiments and spares. An electrostatic deflector will need to be added to turn the beam after the MR-ToF setup into the PUMA chicane vacuum interface in the HIE ISOLDE experimental zone. A new HIE ISOLDE-type diagnostic box containing a Faraday-cup and beam profile scanner is located at the end of the RC6 line. Additional diagnostics will be necessary between the MR-ToF device and the PUMA setup that work in a demanding vacuum pressure environment ($\leq 10^{-8}$ mbar for the MR-Tof device and $\leq 10^{-10}$ mbar at PUMA injection).

Optics for the beam line will need to be designed according to the requirements for PUMA and to the specifications of ISCOOL (the RFQ cooler and buncher after the HRS ISOLDE separator, upstream from the RC6 and PUMA setup) as well as to the requirements of the MR-ToF mass separator for beam purification situated after the ISCOOL and before the PUMA setup. Design and optics simulations will be developed by the EP/SME team in close collaboration with the ISOLDE technical coordination.

8.3 Emittance measurement for the RC6 beam line

With last beam in 2022, some emittance measurements were performed at the end of the existing RC6 line (including the switchyard and a triplet (which will be removed for the creation of the new beam line). Figure 2 shows the set-up of the Allison scanners provided by Triumf.

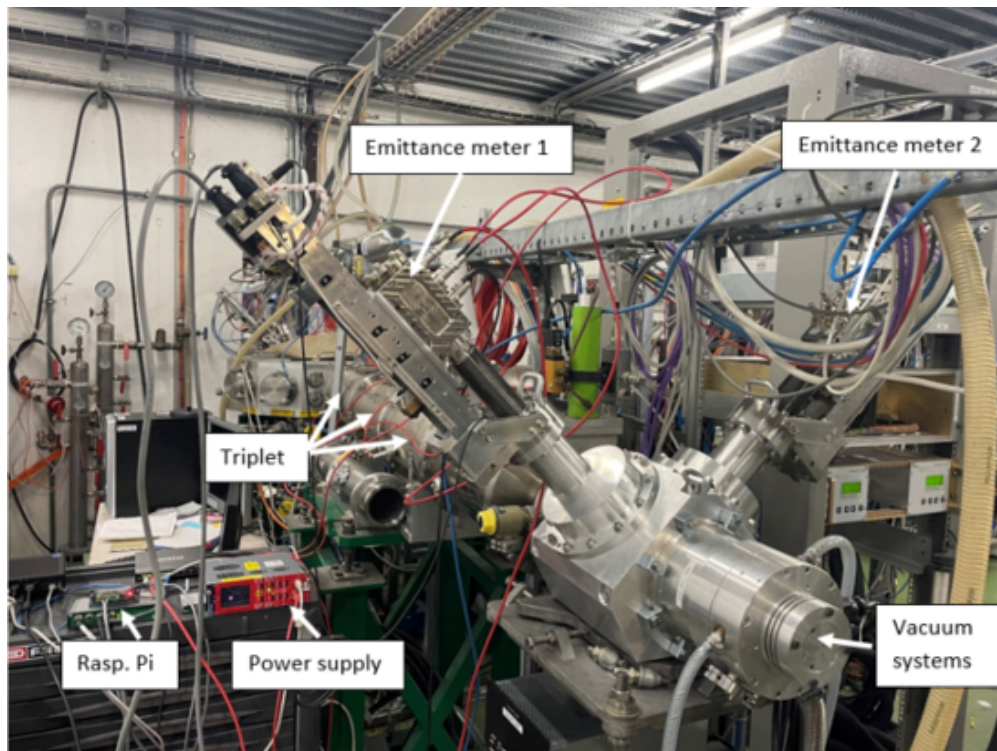Figure 29: Measurement of emittance at the RC6 line, in the two different (rotated) planes (courtesy Niels Bidault (BE/OP)).

On 5th of December 2022, beam was delivered from a surface ionizer source installed in GPS, mainly ^{39}K$^+$ from a dispenser, at 30 keV with an intensity of 80 nA. The beam transmission from the Separator to RC6 was excellent, about 95 %, using the reference setups from OP-ISO. The main results from both

emittance scanners are displayed in the figure 3, with emittance values and Twiss parameters. More measurements will be done with beam in early 2023. With this input the beam optics can be calculated with the first proposed layout (Fig. 31).
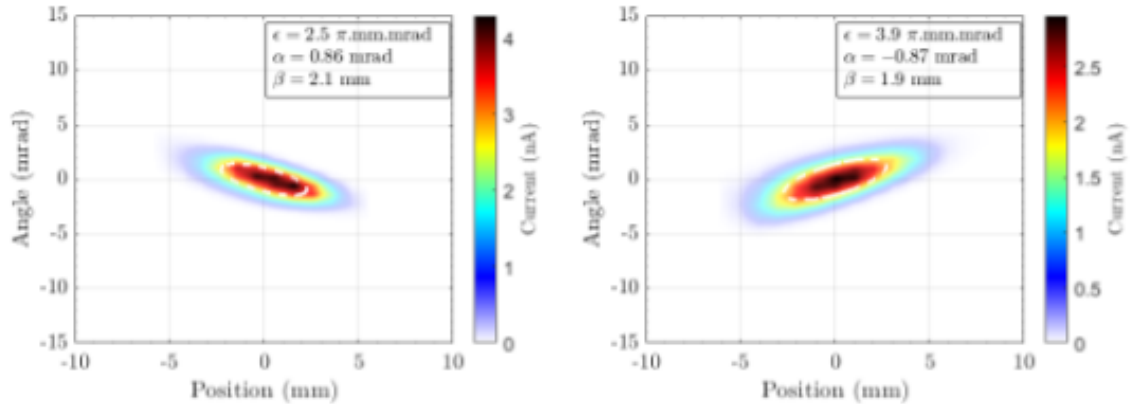

Figure 30: Transverse phase space measured from the emittance-meter 1 (left) and 2 (right).

The main beam elements are (from right to left): switchyard (existing, RC6 no angle, not bakeable), pumping port with valves, 2 magnet modules (ISOLDE spares, not bakeable), 1 Diagnostic box, vacuum valve, a CF160 6-way cross. At this position, there is a parallel branch hosting the Paul trap (PT) and the offline Ion source. Moving these elements out of the direct beam line would ease the vacuum pressure stability of the beam line and allow commissioning of the PT offline (these elements are transferred as built from MIRACLS). This is followed by a vacuum valve, 1 Diagnostic box (HIE ISOLDE type), 2 magnet modules (Elena spares, bakeable), the MR-ToF (from MIRACLS, central chamber to be replaced by a shorter one), a vacuum valve, 2 magnet modules (Elena spares, to be reproduced, bakeable), 1 Diagnostic box (HIE ISOLDE type), a switchyard (existing, bakeable), 1 magnet module (ISOLDE recovery), 1 Diagnostic box (HIE ISOLDE type) and the vacuum valve located at the hand over point to PUMA.
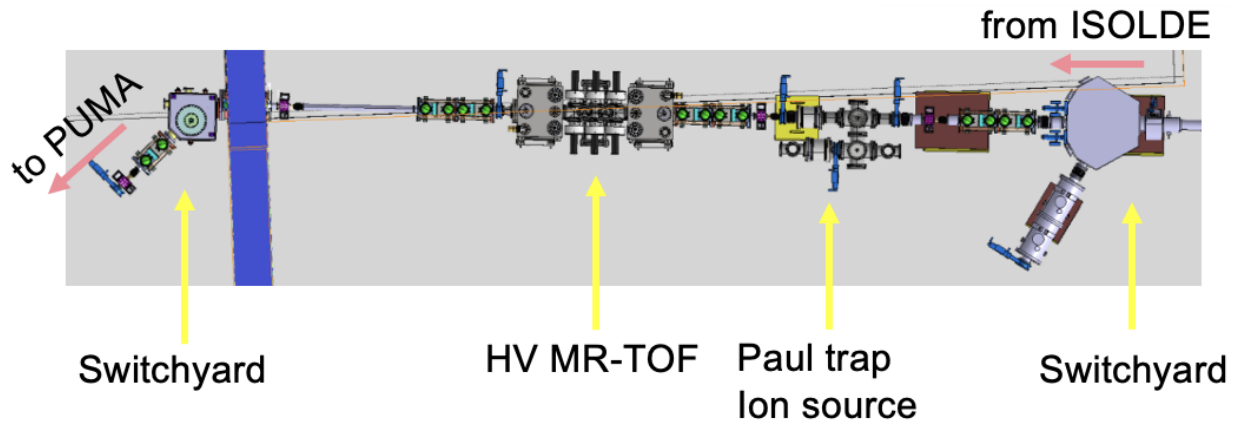

Figure 31: Layout with elements from MIRACLS and recovery form spares. The radioactive beams travel from right to left. The handover point is at the gate valve on the left hand side.

8.4 Vacuum system

The vacuum level required inside the PUMA trap is extremely demanding. At ISOLDE, the standard level of vacuum in the low energy beamlines is better than 10^{-6} mbar upstream and downstream from the IS-COOL. These vacuum conditions set the constraint for the dedicated differential pumping system that will be necessary for PUMA which aims at reduction better than 10^4, from 10^{-6} mbar to better than 10^{-10} mbar at the entrance of the PUMA cryostat with pressures around 10^{-8} mbar in the MR-ToF setup.

A vacuum line between the MR-ToF and PUMA will therefore need to be designed and installed. This transport beam line will need an as much as possible minimized mechanical aperture to reduce the conductance, NEG coating, a bake-out system and differential pumping to achieve UHV at entrance to PUMA ($< 10^{-10}$ mbar). This interface will be built with CERN TE-VSC support.

All the components installed in the beam line need to be previously vacuum tested to ensure they comply the outgassing requirements.

Additional sector valves around the MIRACLS and PUMA setup will be added for protection reasons and to allow PUMA connection and disconnection.

The injection of He in the Paul trap before the MR-TOF can be problematic. Other gases than H_2 and He are more tolerable as they are pumped very efficiently by the trap. The main limitation is the maximum allowable density inside the trap that will define the maximum pressure at the entrance, but no degradation with time should be observed for any gas heavier than H_2. A study to branch off the Paul trap and the offline Ion source could reduce gas pressure issues to the main beam line.

At the end of 2022 the future Paul trap and MR-TOF setup has been installed the experimental station LA2 at ISOLDE. The setup will be commissioning with beam at the beginning of 2023. Taking advantage of the availability of the setup, it is foreseen to measure the helium propagation from the Paul trap through the MR-TOF. The beam line has been modelled and the results are available and coherent with the requirements (pressure <5e-9 mbar) at the handover point between the MR-TOF and PUMA transfer line. The expected helium profile in this configuration is shown in Fig. 32. The measurement of He propagation will be used as a benchmark of the vacuum models used to dimension the pumping needs of PUMA transfer line at ISOLDE to prevent the presence of high He concentration in front of PUMA.
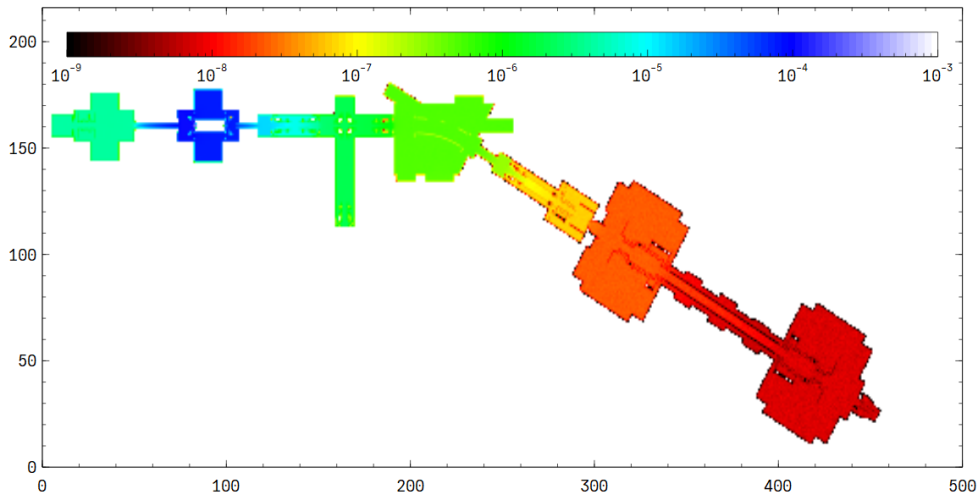

Figure 32: Helium pressure profile in MIRACLS beam line installed at LA2 ISOLDE experimental line.

8.5 Electrical distribution

As described in detail in the ECR 2151516 for the installation of PUMA at the AD the PUMA experiment will have the specificity to be moved back and forth between the AD and ISOLDE. During these transport operations the PUMA trap must be powered without interruption in order not to lose the stored antiprotons inside. The same is valid for any other interruptions such as unforeseen power-cuts while in operation.

Discussions with the EL group point to a single UPS of 100 kVA attached to the PUMA apparatus at all time, that would be connected either to the AD mains, to the truck generator during transport or to the ISOLDE mains. This UPS would then be the interface to the various power supplies and would guarantee no glitches at disconnection-reconnection operations (lifetime of 10 minutes). The transport group has studied the situation in the ISOLDE hall. The position of the new power distribution has been defined with EN-EL. The modifications of the crane to bring the connection point to the crane hook are discussed with a subcontractor and a price inquiry launched. The modification is planned to be implemented during summer 2023.

8.6 Transport

In September 2022 a test was carried out to verify the handling sequence to bring the PUMA experiment inside the ISOLDE experimental zone. The objective of the test was to validate the sequence defined using the 3D models, reaffirming the possibility of access and to identify potential issues.

Figure 33: Handling sequence defined using 3D integration model.

The sequence was performed as expected. Proving that the operation is feasible under the condition of using appropriate tooling that adapts to the available height and allowing the crane hook to be very close to the top part of the experiment.

Some minor issues were identified during the test. Actions will be done to solve them and improve the clearance in the area.

A very important point is to well adjust the centre of gravity of the experiment and to provide appropriate tooling. A new spreader needs to be produced to allow the safe crane operations in ISOLDE (lighter than the one used in AD).

9 Theory

The PUMA theory work package focuses on developing both *ab initio* methods (AIMs) to enable accurate prediction for PUMA experiments and a set of tools for the interpretation of data that can correctly account for the final state interactions (FSIs) of the emitted pions with the cold daughter nucleus. The teams involved are aiming to deliver either landmark predictions using microscopic many-body methods with the associated uncertainties or updated interpretations of past measurements with new standardized tools. This twofold scheme will permit the PUMA collaboration to calibrate the nuclear-antinuclear interaction in very light systems, to deliver nearly model-independent interpretation of data in light systems ($A \leq 16$) where, in addition, FSI tools can be further tested and used to study the spatial extension of the nuclear density in exotic medium-to-heavy systems with minimalist model dependence related to the many-body method able to compute the nuclear density.

In light systems, the data that will be obtained at PUMA and interpreted by AIMs will complement our current understanding of the phenomenon of nuclear halos, extremely loosely bound systems that show universal aspects of few-body systems.

9.1 *Ab Initio* methods for prediction of PUMA data

9.1.1 $N\overline{N}$ interaction

To date, there are various models and/or parametrizations of effective field theory inspired interactions in the $N\overline{N}$ sector. Very little is known about their low-energy behavior in the many-body sector. All previous models, but the one that follows, rely on ad hoc optical potentials to mimic annihilation. Our first aim was to review the discrepancies exemplified in Figure 34 where it can be seen that the global trends in $^{31}S_0$ channel is coherent between the three approaches in contrast to the behavior both at zero energy and around energies where the absorption is large. We have made progress on the update of the Paris $N\overline{N}$ [9] (Paris 2009), in particular we have put in place a smooth regularization towards the origin. The smoothed intersection between the phenomenological short-range and the long-range part of the potential is performed using spline functions. The latter is determined by a state-of-the-art theoretical framework using dispersion relations. The new version avoids derivative discontinuities present at the junction points which make

Figure 34: Comparison of the $p\overline{p}$ $^{31}S_0$ phase shift computed with the Paris 2009 and Kohno-Weise potential [7] with the Nijmegen phase shift analysis [8].

difficult the numerical treatment of loosely-bound antiprotonic atomic states.
Plots comparing the total, elastic, annihilation and charge-exchange cross-section of $p\overline{p}$ between Paris 2009 and its smoothed version show some small differences. These differences could be suppressed by changing slightly the short-range parameters. We are currently working on updating the parametrization to achieve a good fit to the partial-wave analysis of Nijmegen [8]; it should result in a better positions of the quasi-bound and/or resonant nucleon-antinucleon states as required by the study of the light antiprotonic atoms performed in [10].

9.1.2 NCSMC for anti-protonic systems

We will complete our first deliverable (1) by developing the capability to compute with our AIM [11] the scattering of antinucleons by nuclei and the properties of antiprotonic atoms, including the nuclear energy-shift and annihilation half-life (2). We plan to accomplish the calculation of the first low-lying atomic
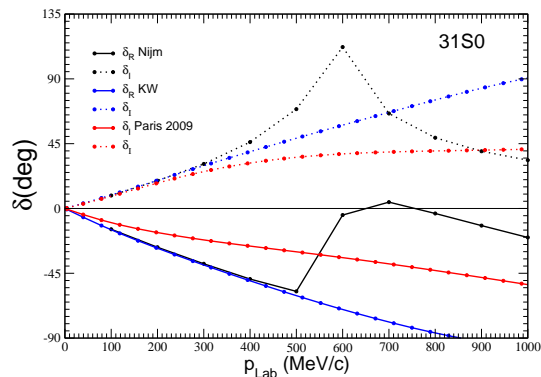
Task #	Description
1	Inclusion of $N\overline{N}$ potentials in our AIM
2	Capability to calculate antiprotonic resonances
3	Application to stable-nucleus antiprotonic atoms
4	Calculation of the first antiprotonic halo system

Table 2: Deliverable for the AIMs work package.

states of antiprotonic H, He, Li, Be, B, and C well-bound isotopes (3), which are two-body problems. Our milestone (4) will be the first *ab initio* computation of the antiprotonic ^{11}Be (n-^{10}Be) atom that will validate our approach to solve a three-body multi scale problem, and is one of the key benchmarks for the experimental program. This system is the simplest case of an antiprotonic halo-nucleus which is both computationally and experimentally accessible. Other antiprotonic atoms made of halo-nuclei (e.g., ^{6}He, ^{11}Li, etc) are of a four-body nature and thus represent a formidable challenge to model. This result will make the connection between data and properties of the ^{11}Be halo nucleus, which despite its apparent simplicity shows very interesting features such as the large observed bound-to-bound E1 emission arising from its extended neutron distribution.

9.2   Data interpretation

The antiproton is first captured in the electron orbital of the target nucleus. The antiproton is in a very highly excited state due to the large mass difference between the antiproton and the electron. To quantitatively understand the process that follows, the distribution of the filled orbitals is very important. Subsequently, the antiproton is deexcited, emitting X-rays and Auger electrons, and transitions to a lower excited state. Then, annihilation occurs when the overlap between nucleons and wavefunctions on the surface of the nucleus increases. At this point, the atomic cascade and annihilation processes are in a competitive relationship. The radial position where annihilation occurs is estimated. Then, antiprotons and nucleons annihilate and pions are emitted. In this process, the final distribution of pions is affected not only by the uncertainty of the distribution of the primordial pions, but also by the effect of the final-state interactions (FSIs). It is very essential in the interpretation of the data how to remove this effect.

Our goal is to determine the ratio of the neutron-to-proton density distribution at the nuclear surface (ρ_n/ρ_p). The scope of this section is to experimentally determine the neutron-to-proton annihilation ratio ($P_{n/p}$).

9.2.1   Analysis method using neural networks

Due to the effect of the FSIs, it is not possible to determine for each annihilation event whether the annihilation partner is a proton or a neutron. Therefore, a so-called statistical method is used to analyze a number of annihilation events to determine what percentage of them are due to annihilation with neutrons (or protons). Under the assumption that the strengths of FSIs are known, previous studies proposed a method to determine $P_{n/p}$ with an error of about 5% for 10^5 annihilation events. By applying a neural network to this problem, we have developed a method that achieves equivalent accuracy with only 10^3 annihilation events. This large performance improvement opens up the possibility of measurement of unstable nuclei with ultra-short lifetimes, such as ^{11}Li.

9.2.2   Approach to the end-state interaction using deep learning

The strengths of FSIs depend not only on the cross sections of the elementary processes but also on the neutron-to-proton density ratio around the annihilation site, which is strongly affected by the nuclear structure of the nucleus of interest. Therefore, the strengths of FSIs are highly dependent on the model, which

causes large systematic uncertainties in the interpretation. A method to derive the strengths of FSIs that does not depend on theoretical models is indispensable. We have developed a new training method that applies the idea of Bayesian statistics to train the deep learning, which is a more complex version of the neural network developed earlier. This method uses simulated data assuming FSIs of various strengths in response to feedback, and can estimate both the strengths of FSIs and $P_{n/p}$ simultaneously from experimental data solely, without assuming any a priori knowledge of FSIs. With this method, $P_{n/p}$ can be determined within a systematic uncertainty of 10% not only for stable nuclei with trivial FSIs, which have been measured in the past, but also for unstable nuclei targeted by PUMA, such as ^{11}Li and ^{132}Sn, where nontrivial FSIs take place.

10 Plans for 2023

The milestones for 2023 are the following:

- modifications (new design of HV Einzel lens, increase of HV to ground distances at air to lower leakage current) to antiproton-beam line for nominal operation,

- full characterization of antiproton beam line and parameter optimization,

- finalization of TPC and long-term (3 months) cosmic ray validation,

- full assembly of trap and cryostat,

- installation of full PUMA at ELENA (offline ion source and experimental apparatus including magnet, traps and detection),

- first trapping of antiprotons,

- vacuum estimate from annihilation rate,

- first trapping of ions,

- installation of low-energy beam line at ISOLDE up to end-over point.

The above milestones, at the exception of the last one, are sequentially connected. Any delay of one milestone would therefore impact the following ones. In the case of a smooth development, we would then proceed with (i) first attempt to transport antiprotons, (ii) stack of antiproton bunches, (iii) transfer of antiprotons from storage trap to reaction trap, (iv) mixing of antiprotons and ions and first measurements.

References

[1] T. Aumann, W. Bartmann, O. Boine-Frankenheim, A. Bouvard, A. Broche, F. Butin, D. Calvet, J. Carbonell, P. Chiggiato, H. De Gersem, R. De Oliveira, T. Dobers, F. Ehm, J. F. Somoza, J. Fischer, M. Fraser, E. Friedrich, A. Frotscher, M. Gomez-Ramos, J. L. Grenard, A. Hobl, G. Hupin, A. Husson, P. Indelicato, K. Johnston, C. Klink, Y. Kubota, R. Lazauskas, S. Malbrunot-Ettenauer, N. Marsic, W. F. O Müller, S. Naimi, N. Nakatsuka, R. Necca, D. Neidherr, G. Neyens, A. Obertelli, Y. Ono, S. Pasinelli, N. Paul, E. C. Pollacco, D. Rossi, H. Scheit, M. Schlaich, A. Schmidt, L. Schweikhard, R. Seki, S. Sels, E. Siesling, T. Uesaka, M. Vilén, M. Wada, F. Wienholtz, S. Wycech, and S. Zacarias, "Puma, antiproton unstable matter annihilation," *The European Physical Journal A*, vol. 58, no. 5, p. 88, 2022.

[2] A. Ishikawa. http://david.attie.free.fr/ILC-TPC/gas/, accessed 19.01.2023.

[3] E. Wallén, "Adsorption isotherms of he and h2 at liquid he temperatures," *Journal of Vacuum Science & Technology A*, vol. 15, no. 2, pp. 265–274, 1997.

[4] F. Chill, S. Wilfert, and L. Bozyk, "Cryopumping of hydrogen on stainless steel in the temperature range between 7 and 18 k," *Journal of Vacuum Science & Technology A*, vol. 37, no. 3, p. 031601, 2019.

[5] Y. Kiwamoto, Y. Soga, and J. Aoki, "Radial transport in magnetized non-neutral plasma driven by rotating wave," *Physics of Plasmas*, vol. 12, no. 9, p. 094501, 2005.

[6] M. Kraus, K. Kormann, P. J. Morrison, and E. Sonnendrücker, "Gempic: geometric electromagnetic particle-in-cell methods," *Journal of Plasma Physics*, vol. 83, no. 4, p. 905830401, 2017.

[7] M. Kohno and W. Weise, "Proton-antiproton scattering and annihilation into two mesons," *Nuclear Physics, Section A*, vol. 454, pp. 429–452, 1986.

[8] D. Zhou and R. G. E. Timmermans, "Energy-dependent partial-wave analysis of all antiproton-proton scattering data below 925 mev/c," *Physical Review C*, vol. 86, p. 044003, 10 2012.

[9] B. El-Bennich, M. Lacombe, B. Loiseau, and S. Wycech, "Paris $N\bar{N}$ potential constrained by recent antiprotonic-atom data and $\bar{n}p$ total cross sections," *Physical Review C*, vol. 79, p. 054001, 5 2009.

[10] B. Loiseau and S. Wycech, "Extraction of baryonia from the lightest antiprotonic atoms," *Physical Review C*, vol. 102, p. 034006, 9 2020.

[11] P. Navrátil, S. Quaglioni, G. Hupin, C. Romero-Redondo, and A. Calci, "Unified *ab initio* approaches to nuclear structure and reactions," *Physica Scripta*, vol. 91, p. 053002, 5 2016.